UNIVERSITY OF SOUTHAMPTON

Extreme Ultraviolet Ptychography of Young Mouse Neurons

by

Jieyuan Fan

Thesis for the
degree of Master of Philosophy

in the
Faculty of Natural and Environmental Sciences

September 2017

Abstract

Ptychography is a lensless, phase-sensitive, diffraction-imaging technique that can provide high-resolution images of non-crystalline objects. Iterative phase-retrieval algorithms replace the role of lenses, allowing reconstruction of the object image. The lensless nature of ptychography provides a major advantage for use with extreme ultraviolet and soft x-ray wavelengths, which are an important spectral region for high-resolution microscopy but difficult to manipulate with lenses.

In this project, 7DIV (days *in vitro*) mouse hippocampal neurons are imaged for the first time using EUV ptychography at the University of Southampton and on the Artemis laser at the Central Laser Facility (Didcot, UK) at a wavelength of 29 nm. The EUV radiation is generated via high harmonic generation through argon gas. The images show fine structures that are well defined and not resolved via conventional microscopy, achieving up to 102 nm resolution over a 42 μm field of view in both phase and amplitude. The ptychography imaging experiment is also carried out using a projected pinhole in place of a physical pinhole, resulting in successful, albeit poorer reconstruction. Compositional analysis on the reconstructed images is also explored, by considering the complex refractive index, $n = 1 - \delta + i\beta$. The ratio δ/β, which is unique for different materials, can be calculated from the image data, and can provide some insight on spatial distribution of content across a structural feature.

Acknowledgements

I would like to express my gratitude to my supervisors Professor Jeremy Frey and Dr Bill Brocklesby for tremendous amounts of guidance, patience, and encouragement throughout the entirety of this project, and for the opportunity to work on a project that has challenged me to learn and widen my skillset. Special thanks also go out to Dr Russell Minns for all his advice and patience.

I would also like to extend my gratitude to Dr Joanne Bailey, who cultured and prepared the neuron samples imaged in this project, the Artemis laser facility staff scientists, for their support in carrying out ptychography experiments on the Artemis beamline, Professor John Chad and Dr Katrin Deinhart of the Institute for Life Sciences at the University of Southampton, for sharing their knowledge on mouse hippocampal neurons, and Dr Stuart Boden, who fabricated the FIB-milled samples used in this project.

Peter Baksh and Michal Odstrcil, whose extensive work on the x-ray ptychography project form the groundwork for much of my research, have been generous in sharing their knowledge and giving me guidance from the start; I am deeply grateful for their kind mentorship. Michal has performed numerous reconstructions throughout the duration of this project, for which he is credited in my thesis, and I am grateful for his time and effort.

My colleague Magdalena Miszczak provided much help and company while working in the lab, for which I am very thankful. Many thanks also go out to Charlie Pooley and Haoyan Lu for their help and company, and the rest of the Ultrafast x-ray group for their help in the project.

Finally, I would like to thank my family for their endless support and patience.

Contents

List of Figures

Chapter 1

Introduction

The ability to image biological specimens is hugely benefitted by advances in imaging and microscopy technologies; in turn, the desire to study even smaller structures at better resolution and higher definition provide a large driving force for the development of these techniques.

Lensless imaging, in particular, is an area of interest as the shorter wavelength radiation – such as extreme ultraviolet, soft x-rays and hard x-rays – necessary for high-resolution imaging are characteristically difficult to manipulate with lenses; lenses are often not a viable option for x-ray microscopy. Lensless microscopy techniques can provide high-resolution images with much less reliance on high-quality optics, which are accompanied by aberrations and fabrication difficulties [1].

Coherent diffractive imaging (CDI) techniques are a prominent type of lensless imaging technique that can provide nanoscale images of objects, and they have a notable advantage in that they are able to solve the phase problem. In CDI, the diffraction pattern of a sample is collected and computational algorithms – often called reconstruction algorithms or phase retrieval algorithms – reconstructs the information about the phases, from which an image of the sample can be formed, as such, replacing the role of the lens in conventional microscopy. CDI is suitable for non-crystalline samples – in contrast to x-ray crystallography, a powerful technique that can provide up to atomic resolution of structures but requires crystalline samples. In this way, CDI opens up lensless imaging techniques to a much wider variety of sample types, biological and non-biological. CDI microscopy in the x-ray spectral region is becoming an established microscopy technique employed at large-scale coherent light facilities [2].

Ptychography is a scanning CDI technique that allows for an extended aperiodic sample to be imaged. The work in this project is part of ongoing research by the Ultrafast x-ray group at the University of Southampton in achieving and developing extreme ultraviolet (EUV) ptychography and continues the effort to image young mouse hippocampal neurons. In the ptychography process, the neuron samples are scanned relative to a coherent EUV beam, the scatter pattern at each scan position is collected, and an iterative reconstruction algorithm is used to generate the image of the sample from these scatter patterns. Adjacent scan positions have overlapping regions, and the repeated sampling provides a key constraint in the reconstruction process. The coherent EUV beam is generated by high-harmonic generation.

The following sections of this chapter give an overview of the project, and discuss the context of biological imaging, the EUV spectrum and lensless imaging, and how ptychography at the EUV wavelengths come into play.

Ptychography and high-harmonic generation principles are discussed further in Chapter 2 and Chapter 3 respectively, and experimental information is presented in more detail in Chapter 4. The results are presented and discussed in Chapter 5, and conclusions and recommendations for future work are summarised in Chapter 6.

1.1 Project overview

In this project, extreme ultraviolet (EUV) ptychography is used to image young mouse hippocampal neurons that have been cultured for 7 days *in vitro* (DIV).

Coherent EUV is generated via high-harmonic generation (HHG), a highly non-linear process. HHG is described in more detail in Chapter 2. An infrared (IR) beam of ~800 nm is focused into a gas cell to generate a spectrum of EUV, using argon gas as the generation medium. After generation, thin aluminium layers are used to filter out the IR beam. The 29th harmonic – corresponding to 29 nm wavelength beam – is selected via a MoSi multilayer focusing optic; the 29 nm beam is used as there is a contrast between carbon and water transmission at this wavelength. The 29 nm beam is focused through a pinhole of 5-10 μm radius, before passing through the sample. The samples are neurons cultured and fixed on a silicon nitride (Si_3N_4) membrane of 500 μm thickness, and scatter patterns are collected using a cooled CCD camera. Sections 3.1, 3.2, and 4.1.3 describe the laser system used, the experimental setup, and neuron preparation respectively.

The size of the probe beam is small compared to the sample dimensions, and during ptychography, the sample is scanned relative to the beam and diffraction patterns are collected at each scan position. The overlaps between consecutive scan positions allow reconstruction of the image, which was performed by Michal Odstrcil, another member of the Ultrafast x-ray group at Southampton. Ptychography is a phase-sensitive technique, discussed briefly in Section 6, and the results from reconstruction include both intensity and phase information, the latter of which is lost in most other diffraction-based techniques – by considering the complex refractive index of materials this allows analysis that give insight to composition.

Over the course of this project, the work done continues the work of group members Peter Baksh and Michal Odstrcil who previously successfully imaged 14DIV mouse hippocampal neurons [3] [4]. Much work was done to troubleshoot and maintain the beamline and equipment. Compositional analysis of the neurons based on the data from reconstruction is also explored and discussed in Chapter 4.

In addition to demonstrating the capabilities of ultrafast EUV generation, tabletop x-ray microscopy, developments in ptychography and image reconstruction, these experiments also aim to contribute towards the development of ultrafast x-ray microscopy for potential applications such as imaging protein assemblies in the gaseous state. The techniques and methods used in successfully performing EUV ptychography at 29 nm may translate if radiation of other wavelengths, such as soft x-ray wavelengths, are used.

1.2 Biological imaging

The desire to study increasingly smaller biological samples and structures at higher resolution provides a great driving force for the development of microscopy and imaging techniques.

In conventional optical microscopy, the sample is illuminated by visible light in the focal plane of the objective lens, and the refracted and diffracted light form a real image. Often, an eyepiece – a further lens or groups of lenses – magnifies the image to be viewed by eye, or via a digital camera. However, the resolution of light microscopes is fundamentally limited by the wavelength of the radiation used. This resolution limit is also often referred to as the diffraction limit or diffraction barrier, in that objects separated laterally by a distance less than half the wavelength of the illuminating radiation cannot be distinguished. Ernst Abbe proposed this limit in 1873 [5], where light with wavelength λ travelling in medium with refractive index n and converging to a spot of half-angle θ will form a spot with radius:

$$n = \frac{\lambda}{2dsin\theta} = \frac{\lambda}{2NA} \tag{1.1}$$

where $n sin\vartheta = NA$, the numerical aperture, the maximum acceptance angle of diffracted, reflected or refracted radiation that can be measured by a detector, and d is the distance between lattice planes. In modern optics, use of oil immersion lenses can achieve NA of up to 1.6.

The invention of electron microscopy was significant in overcoming the barrier to higher resolution imposed by the diffraction limit of visible light, and electron microscopy is currently the most commonly used method for imaging in the nanoscale regime. The wave-particle duality of electrons means that electrons can behave like waves and be used for imaging. Matter waves have associated wavelength, known as the de Broglie wavelength, λ, related to momentum, p, through the Planck constant, h, given by:

$$\lambda = \frac{h}{p} \tag{1.2}$$

The high resolution provided by electron microscopes is due to the smaller de Broglie wavelength of electrons. Scanning electron microscopy (SEM) and transmission electron microscopy (TEM) are two of the most widely used forms of electron microscopy.

SEM uses a focused beam of electrons to probe the surface of a sample, with the detection of secondary electrons liberated from the sample surface and back-scattered electrons from the electron beam providing information about the surface topography and composition of the sample. Unlike in an optical system, the resolution of SEM is limited not by diffraction limit but by the energy of the electron beam, and is often in the range of several nanometres. Typical resolutions of SEM are on the order of nanometres.

In TEM, a high-voltage electron beam is used to illuminate the sample, and an image is formed from the interaction of electrons with the sample as the beam is transmitted through the specimen. The typical resolution of TEM an order better than SEM, and picometer resolution has even been achieved by accelerating electrons to high enough velocity [6].

Cryogenic electron microscopy, cryo-EM, is a steadily developing technique that has picked up considerable momentum in recent years, and provides a solution to several of the problems faced by SEM and TEM for biological imaging. It does not require stained or fixed samples, which allows many biological specimens to be viewed in a near-native state. Samples for cryo-EM are vitrified in a layer of glass-like ice and imaged at liquid nitrogen or helium temperatures, which reduces the radiation damage considerably compared to at ambient temperatures – thus, a much higher electron dose can be used for the same amount of radiation damage. Near-atomic resolution has been achieved with cryo-EM, and with advances in microscope design, hardware, imaging processing algorithms and automation, it is a highly effective technique for studying the structure of cells, viruses, and proteins at molecular resolution. Cryo-EM can also provide 3D information [7].

For imaging surfaces at the atomic level, scanning probe microscopy techniques, such as atomic force microscopy (AFM) and scanning tunnelling microscopy (STM, are often employed. AFM and STM are commonly used for material roughness measurements. In these experiments, the tip of a physical probe raster scans over the surface of the sample and values are recorded at discrete points throughout the scan to produce the final image. Unlike many other forms of microscopy, the resolution of AFM and STM are not diffraction limited as no form of radiation is used. There is also no need for vacuum imaging conditions, and experiments can be carried out in ambient conditions or even submerged in a liquid vessel. However, these techniques are unsuited for studying buried structures such as cell organelles or structures in solution such as proteins.

Of the drawbacks of electron microscopy, the vacuum environment and extensive sample preparation required are significant ones for biological imaging. As with many techniques for high-resolution imaging, SEM and TEM both require imaging be carried out under vacuum, as electron absorption by air would be far too high to generate signal from the sample. As a result, samples are instantly dehydrated – this can cause structural collapse in samples such as cells, organelles, and tissue.

To prevent accumulation of charge, SEM samples require an electrically conductive surface. Non-conductive samples are often coated with gold or heavy metal alloys for SEM analysis. The sputter-coating process that is often used in SEM sample preparation can often damage fragile specimens or alter their structure. TEM often necessitates harsher fixing, including embedding the sample in a resin in order to section the sample into ultra-thin slices; coating with a conductive material may also be necessary. Biological samples typically also require staining with heavy metals to enhance contrast or reduce irradiation damage. As such, electron microscopy samples are far removed from *in vivo* conditions.

Radiation damage can also be a significant problem for high-resolution microscopy techniques, as shorter wavelength radiation is high in energy. The high-energy electron beam used in SEM and TEM can cause sample damage due to irradiation. Electrons interact strongly with the sample, depositing large amounts of energy into the sample – samples can reach temperatures close to 100°C in both SEM and TEM, which is sufficient to cause significant damage to biological samples. Although images of unstained samples can be obtained at lower low electron doses, the low electron dose often results in poor signal-to-noise ratio as unstained biological samples are primarily composed of low atomic number elements that scatter electrons only weakly [8]. In practice, for cryo-EM there are also dosage limits before samples degrade. The cryogenic conditions can also create artefacts, and it remains a technique for studying stationary structures.

Although ptychography using EUV radiation also requires vacuum conditions due to high attenuation of EUV in air, considerably less sample treatment is needed. The neuron samples imaged by EUV ptychography in this project have been fixed using paraformaldehyde, and care has been taken to dry the samples gradually in order to minimise structural collapse. No further sample treatment procedures were used.

1.3 Extreme ultraviolet and soft x-ray spectrum

The main context of this project is extreme ultraviolet radiation, as the radiation wavelength used in this project falls within this region of the EM spectrum. Closely related to EUV is soft x-ray radiation, which occupies the immediately adjacent region of the EM spectrum to EUV, and much of the discussion will be in the context of both EUV and SXR.

The electromagnetic (EM) radiation spans a wide range of frequencies and their corresponding wavelengths. One of the last regions of the EM spectrum to be explored and developed is that of the extreme ultraviolet (EUV) and soft x-rays (SXR), which lie between ultraviolet and x-ray radiation. The extreme ultraviolet region extends from photon energies of about 30 eV to 250 eV, which correspond to wavelengths of about 5nm to 40nm. The soft x-ray region spans from about 250 eV to several keV.

Light can interact with matter in several ways, and in the case of microscopy the absorption, scattering, diffraction, and refraction of radiation need to be considered. Absorption of a photon of energy $h\nu$ promotes a particle from a lower energy state to a higher energy state, and various spectral regions have energies associated with different energy transitions.

The EUV and SXR spectral regions are characterised by the presence of the primary atomic resonances and absorption edges of several elements with low atomic number, Z, that lie within this region. The primary absorption edges are often called K-, L-, and M-absorption edges, which are associated with the removal of a core electron by photoabsorption from the most tightly-bound atomic states – orbitals of principal quantum numbers $n = 1$, $n = 2$, and $n = 3$ respectively. Notably, the K-absorption edges of carbon, oxygen, and silicon, as well as the L-absorption edge of silicon lie within the combined EUV and SXR region.

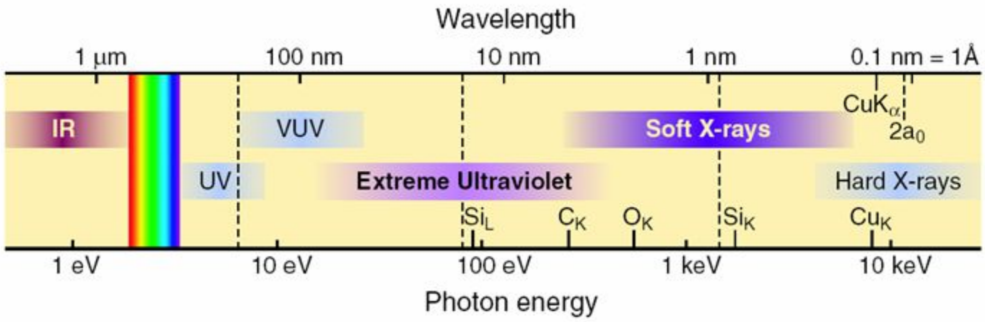

FIGURE 1: Electromagnetic spectrum showing extreme ultraviolet (EUV) and soft x-ray (SXR) spectral regions as well as absorption edges for silicon, carbon, oxygen within the EUV-SXR spectral region. Figure taken from Attwood [9].

As there are numerous absorption edges that lie in the EUV-SXR region, there is a high degree of absorption in all materials in this region. This is a marked difference from lower or higher photon energies (such as UV/VIS or hard x-ray regions) where many materials are 'transparent' to incident radiation, which leads to a key benefit of not requiring vacuum isolation techniques in general. As air and all materials are highly attenuating at EUV wavelengths, performing experiments under vacuum is a necessity when using EUV radiation. However, this also provides the potential of sensitive elemental and chemical identification. The 'water window', a region where water is relatively transparent compared to carbon, also lies within this region which further adds to the opportunities presented for spectroscopy and imaging for the biological and life sciences; this is discussed briefly in the following section.

Scattered light also needs to be considered in microscopy. Scattering is a term used to describe a deviation of radiation from a straight trajectory upon interaction with matter. This redirection is due to the interaction of the electric fields of the incident light and atoms of the scattering object. The oscillation of the scattering object emits radiation. Light can be scattered in all directions and different frequencies, and the distribution is determined by the structure of the scattering object. Light that is scattered in the opposite direction of incident light is known as reflection.

The superposition of scattered waves gives rise to diffraction, and if the scattering object is highly ordered, the interference of the diffracted waves forms a diffraction pattern with periodicity that may be used to deduce the relative positions of atoms in the object, such as in x-ray crystallography. The angles for diffraction from a crystal lattice with period d are given by Bragg's law:

$$2dsin\theta = n\lambda \quad (n\ is\ a\ positive\ integer) \qquad (1.3)$$

Light scattered in the forward direction, upon combination with the incident beam, gives rise to the phenomena of refraction. This manifests as a change in phase velocity as a wave propagates through a material. The refractive index, n, of an optical medium is often given as

$$n = \frac{c}{v} \tag{1.4}$$

where c is the speed of light and v is the phase velocity of light through the medium. However, to account for the attenuation of light passing through a medium, it is useful to consider the complex refractive index, expressed as

$$n = \alpha + i\beta \tag{1.5}$$

where α is the real part, which describes the change in phase velocity of the wave, and β describes the attenuation properties of the material. This constant is also known as the extinction coefficient.

In the high-energy photon regime, of which the EUV/SXR region is part of, the real part of the refractive index is close to unity. As a result, for the EUV/SXR region the refractive index is often written as

$$n = 1 - \delta + i\beta \tag{1.6}$$

where δ and β are generally small. δ and β are expressed in terms of real and imaginary parts of the complex atomic scattering factor, $f^0(\omega)$:

$$\delta = \frac{n_a r_e \lambda^2}{2\pi} f_1^0(\omega) \tag{1.7}$$

$$\beta = \frac{n_a r_e \lambda^2}{2\pi} f_2^0(\omega) \tag{1.8}$$

where

$$f^0(\omega) = f_1^0(\omega) - i f_2^0(\omega) \tag{1.9}$$

The complex refractive index, as well as the constants δ and β are referred to later on in this thesis, in Chapter 4, on analysis of data.

1.4 Biological considerations and the water window

The interest in biological imaging using radiation in the EUV and soft x-ray region often requires consideration and balance between both wavelength and photon energy. The illuminating wavelength dictates the resolving power, while the energy deposited per unit mass – dose – can cause damage to biological samples.

The soft x-ray wavelengths are in the range of the dimensions of biological macromolecules, which makes soft x-rays suitable for resolving these structures of interest. Very notably, the SXR region contains the water window, from around 2.33 nm to 4.40 nm. Within the water window, water is effectively transparent, thus providing a natural contrast mechanism between water, the major component of media such as cellular cytosol, and carbon, which is present in all organic material including proteins and lipids. This is because of the presences of the 284 eV carbon K-edge and 534 eV oxygen K-edge that bookend the water window. Figure 2 shows this contrast in terms of the absorption length for carbon and water in the water window – for 10 μm of water, the typical thickness of a cell, carbon has a far shorter absorption length. This natural contrast at high spatial resolution is particularly attractive for the prospect of imaging without fixation, and without removal of water. For example, imaging of whole cells in their growing medium or large protein assemblies in cytosol or buffer medium may be possible. This would be a significant advantage for understanding biochemical structures and cellular processes. However, the dosage effects in the SXR region may be non-trivial. Unlike in the hard x-ray region where sample absorption is low, photons in this spectral region have sufficient energy to ionise atoms and break molecular bonds, which can cause chemical and structural damage.

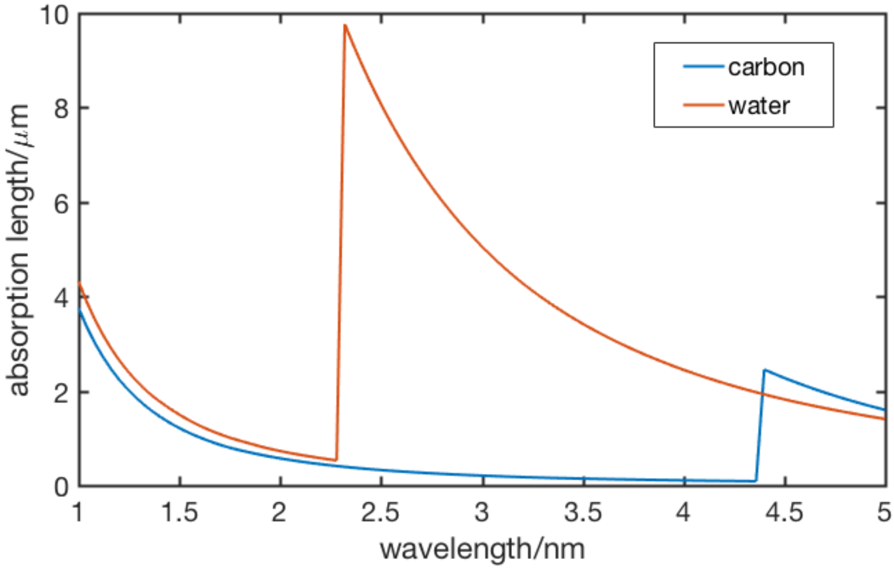

FIGURE 2: Graph of absorption length against wavelength for carbon and water in the spectral region called the water window. The 284 eV carbon K-edge (4.40 nm) and 534 eV oxygen K-edge (2.33 nm) lie within this region, resulting in a large difference in absorption length where water is relatively transparent

compared to carbon. This provides strong natural contrast in biological samples. Data obtained from the CXRO calculator [10]; figure recreated from [3].

Compared to the soft x-ray region, the extreme ultraviolet (EUV) spectral region has fewer characteristics that lend it to biological imaging. However, there is unexplored potential for biological imaging using EUV radiation. Although the wavelength is longer than soft x-rays, coherent diffractive imaging resolutions of 22 nm have been achieved using EUV [11], which is approaching the resolution power of SEM. There are also two regions, around 5 nm and 29 nm, where there is high contrast between carbon and water that makes it suitable for probing biological or organic samples that are carbon-rich; this is shown in Figure 3.

A main drawback to imaging in the EUV region is the high attenuation by air, which necessitates a vacuum environment for all experiments using EUV radiation. Similar to electron microscopy techniques, the vacuum environment may be suitable for investigating isolated samples, but in general is not conducive for imaging biological specimens as they are far removed from a native environment, and imaging in real-time is not possible. Fixation procedures are used in this project in order to image neuron cells by EUV ptychography (described in Chapter 4), though the fixation is less harsh compared to what is typically used from electron microscopy. Additionally, care must be taken in maintaining vacuum environments.

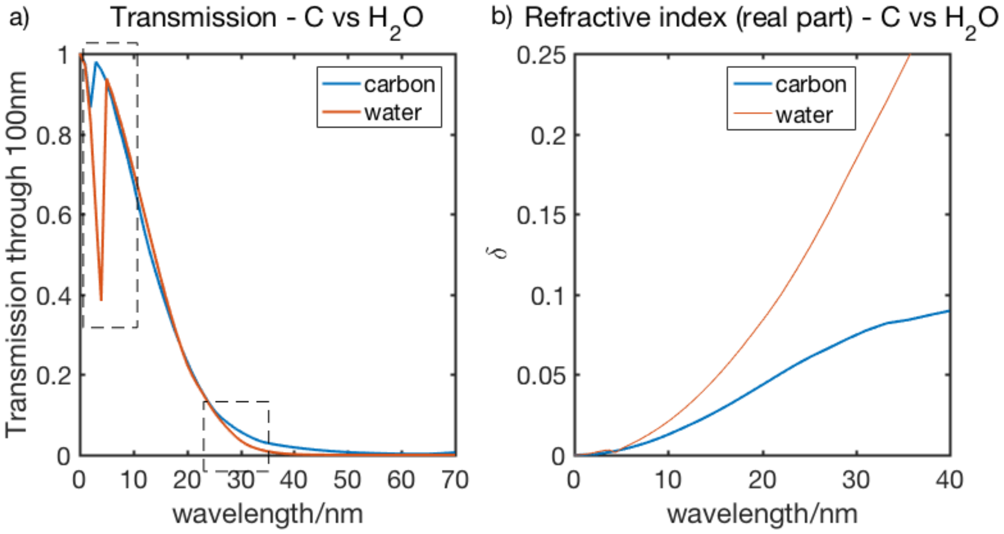

FIGURE 3: (a) Graph of transmission against wavelength through 100nm for carbon and water for EUV-SXR wavelengths. There is notable contrast in the regions of 5nm and 29nm, which are indicated by the rectangles formed from dashed lines. (b) Graph of the real part of the refractive index, δ, against wavelength for both carbon and water for EUV-SXR wavelengths. The real part of the refractive index is responsible for phase change. This allows for phase contrast between water and carbon. Data obtained from the CXRO calculator [10]; figure recreated from [3].

As the photon energy of EUV radiation is lower than that of soft x-rays, the sample dose is minimised when using EUV radiation for biological samples. Table-top generation of coherent EUV is also a more routine process, which allows table-top EUV ptychography to be possible. This can make EUV experiments more easily accessible; high-flux coherent soft x-rays are usually generated at free electron laser (FEL) facilities.

Chapter 2

Ptychography

X-ray ptychography combines raster scanning x-ray microscopy with the principles of coherent diffractive imaging. It is a microscopy technique that offers a solution to the phase problem, and it is not limited by the fabrication challenges of x-ray optics or isolated sample preparation. This chapter gives background on the background and details of ptychography and high harmonic generation, the process used to generate coherent extreme ultraviolet radiation for ptychography.

2.1 Coherent diffractive imaging principles

Coherent diffractive imaging (CDI) is a lensless microscopy technique that is able to obtain high-resolution images on the nanoscale by probing specimens with a coherent source of radiation (often x-rays or electrons), with the diffraction pattern providing magnitude information, and phase information recovered with iterative algorithms and oversampling, allowing the reconstruction of the object image. This solves the 'phase problem' that most diffraction-based techniques such as crystallography are unable to. CDI also lends well to aperiodic samples, unlike crystallography.

As no lenses are employed in CDI, the images are aberration-free and resolution only limited by diffraction and exposure, and the capabilities of the reconstruction algorithms. Various methods based on CDI have been developed, and ptychographic CDI – commonly known as ptychography – which is the technique employed in this project.

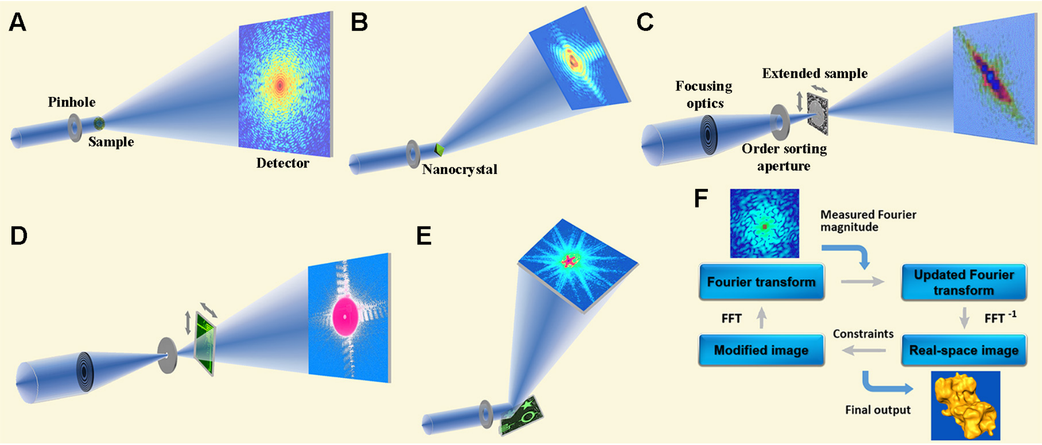

FIGURE 4: Figure from [13]. Figure shows schematics of various CDI methods and iterative phase retrieval algorithms. (A) shows plane-wave CDI, where a plane wave illuminates a sample and the diffraction is measured by a detector. In Bragg CDI (B) the diffraction pattern surrounding a Bragg peak from a nanocrystal is measured. Ptychographic CDI is shown in (C), where an extended sample is scanned through a coherent illuminating probe in a series of partially overlapping positions, and the diffraction pattern is collected. In schematic (C), a Fresnel zone plate is used to focus the beam; this can be achieved with an aperture or other focusing optics. (D) shows Fresnel CDI, where the Fresnel diffraction pattern of a sample is measured by the detector. Reflection CDI is shown in (E), where a coherent beam is reflected off a sample and the diffraction intensity around the beam is collected by a detector. (F) shows a schematic for phase retrieval algorithms.

CDI-based methods provide several significant solutions to imaging at high-resolution, most notably the phase problem that is associated with diffractive imaging. Related to this is the ability to forego the use of lenses, which circumvents difficulties with optics for short wavelengths, though drawbacks do exist. These are discussed briefly in this section. Ptychography and several algorithms used in ptychography reconstructions are also described briefly.

2.2 Overview of ptychography

Ptychography, sometimes known as scanning or ptychographic coherent diffractive imaging, emerged as a generalisation of conventional CDI that could be suitable for samples with significant lateral extent, by shifting the probe relative to the object and collecting measurements of scatter pattern at each position. The name ptychography comes from the Greek word *ptycho*, meaning 'to fold', which represents the characteristic overlapping scanning positions.

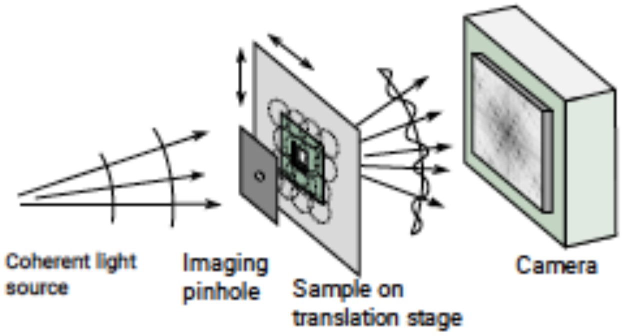

Figure 5: Figure taken from [4]. Schematic of a typical arrangement for ptychography. A coherent light source is incident upon an aperture just upstream of the sample, which is scanned laterally through a series of partially overlapping positions relative to the illuminating beam. The scatter pattern at each illuminating position is oversampled and recorded by a detector.

Arrangements for ptychography typically consist of a coherent beam of radiation that passes through a pinhole mounted upstream from an object, such that the aperture defines the illuminating radiation upon the sample – a pinhole defines a tophat function. The scattered radiation is collected by a detector further downstream – often a charge-coupled device (CCD) – and multiple scatter patterns are collected as the sample is scanned relative to the probe beam. Sufficient overlap between adjacent probe positions results in redundancy in the data acquired [14] – this is typically 60% overlap –and this allows for a very robust reconstruction and phase retrieval method that is also able to correct for systematic errors [15], [16], [17]. This can even be applied to 3D imaging [18].

The scatter patterns collected are then processed using reconstruction algorithms – also known as phase-retrieval algorithms – that are iterative and are able to recover the phases, from which an image of the sample can thus be obtained.

The scanning process of ptychography allows samples of larger size and shape to be imaged, effectively giving the method an extremely large field of view. In practice this may be accompanied by the drawback of long total scan times and the need for beam stability for the duration of the scan.

2.3 Lensless benefits and the phase problem

CDI methods use oversampling to enable phase-retrieval algorithms to solve the phase problem. In the context of imaging, this provides a key benefit to unshackling image formation with the need for suitable and sufficiently high-quality lenses. This is particularly relevant for wavelengths in the EUV and SXR spectrum, as described in Chapter 1.

The phase problem refers to the loss of phase information when measuring intensity of EM radiation. Light detectors, such as CCD cameras, only measure the intensity of light, I, which is related to the square of the modulus of the wave. This means that the measurements give an incomplete description of the electric field.

$$I = E_0 e^{-i(kx+\phi)} E_0 e^{-i(kx-\phi)} \tag{2.1}$$

where E_0 is the amplitude of the field, k is the wavenumber, and ϕ is the phase.

In the situation where it is only possible to record a property related to the intensity of the Fourier transform of the object, the creation of an image from such data leads to the classic phase problem. For conventional optical microscopy using visible light, there is little need to solve the phase problem as lenses are used to focus the illuminating radiation, and phase information is retained during refraction.

However, the use of lenses does not lend well to x-ray microscopy if the high resolution that these short wavelengths have the potential for is to be exploited. This is because fused silica, often used to make lenses, has a resonance frequency close to that of high-energy photons, so the material interacts weakly with the photons, and there is very little alteration to phase (Figure 6). Yet, the purpose of lenses is to apply varied amounts of alteration to the phase as the lens thickness varies – the spherical curvature of an objective lens in microscopes is the physical property that focuses light. In order for a lens to focus x-ray photons, it would have to be manufactured to be very thick, which would conversely lead to higher absorption losses in the material.

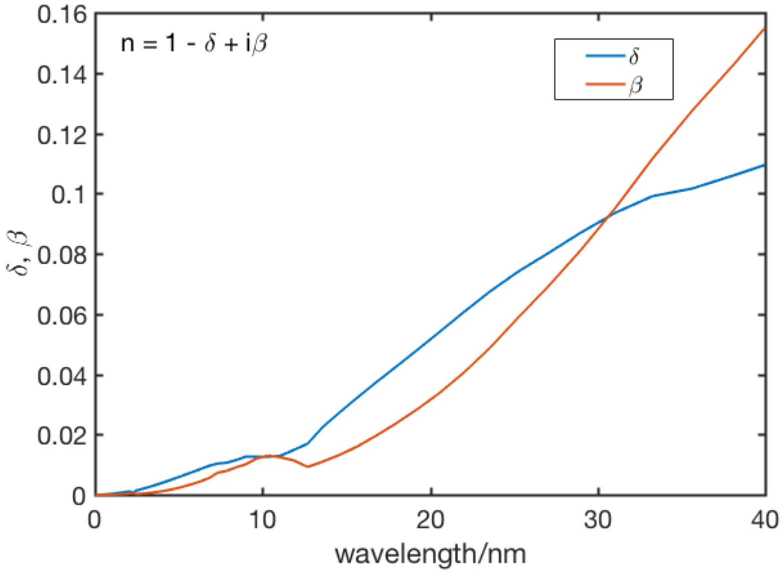

FIGURE 6: Graph showing δ and β of the complex refractive index as a function of wavelength for fused silica. The variation of δ and β in the EUV-SXR wavelength region is very small, so a lens to focus EUV wavelengths will need to be very thick in order to achieve sufficient phase shift in fused silica. However, the absorption losses in a thick optic would be high. Data for this figure generated from CXRO database [10], figure recreated from [3].

A commonly used method to focus high-energy radiation is to use a Fresnel Zone Plate, a structure that has a pattern of concentric rings with decreasing spacing moving away from the centre. The FZP relies on diffraction to focus radiation. FZP are used in Fresnel CDI, where an order-sorting aperture selects the first-order diffracted wave to illuminate the sample.

However, there remain common problems to all the methods for focusing high-energy radiation. Firstly, there is often poor efficiency, as would be the case with a thick fused silica optic. The overall transmission efficiency of FZP can be poor, as transmission over the rings of the plate is low. The use of order-sorting apertures further reduces efficiency.

There is also an inherent problem of imperfections on the scale of the illuminating wavelength for all optics for high-energy photons. Manufacturing defect-free, high quality optics for short wavelengths can be technically difficult and expensive.

2.4 Coherence

Ptychography requires a degree of coherence from the illuminating radiation used. Coherence describes how well a wave correlates with itself in both space and time, and a light field is coherent if there is a fixed relationship between the electric field at different positions or different times. For a beam with good coherence, the intensity, I, of a diffracted wave is given by equation 2.2:

$$I = \left|\sum_i u_i(x,t)\right|^2 \tag{2.2}$$

where u_i represents the wave scattered from point i. Conversely, equation 2.3 is used when calculating the diffracted intensity for a completely incoherent wave.

$$I = \sum_i |u_i(x,t)|^2 \tag{2.3}$$

The mutual coherence function, given in equation 2.4, is often used to quantify coherence between two points, x_1 and x_2, separated by time τ:

$$\Gamma(x_1, x_2, t+\tau) = \langle E(x_1,t)E^*(x_2,t+\tau)\rangle \tag{2.4}$$

where the notation $\langle$ and $\rangle$ indicate the time average. This can be normalised and expressed as:

$$\gamma(x_1, x_2, t+\tau) = \frac{\langle E(x_1,t)E^*(x_2,t+\tau)\rangle}{\sqrt{I(x_1,t)}\sqrt{I(x_2,t+\tau)}} \tag{2.5}$$

where I is the intensity at a given point. The mutual coherence function is equal to 1 for a perfectly coherent field and equal to 0 for an incoherent field. A wave may also have partial coherence if its mutual coherence function is between 0 and 1. The length and time over which a wave exhibits coherence are often expressed as L_{coh} and τ_{coh} respectively.

When describing coherence properties of the wave, there are both spatial and temporal coherence to consider. Spatial, or transverse, coherence refers to correlation – a fixed phase relationship – between different points, separated spatially, across the beam profile. It describes how uniform the phase of a wave front is. Full spatial coherence can be achieved with a spherical wavefront. Attwood [9] derives a relationship with which to quantify spatial coherence, first by approximating the laser as a point source with diameter $d = 2\Delta x$, where Δx is the uncertainty in position, with uncertainty in momentum represented by $\Delta\mathbf{p}$ and using observation half angle θ. Using Heisenberg's uncertainty principle,

$$\Delta x \Delta\mathbf{p} \geq \frac{\hbar}{2} \tag{2.6}$$

since momentum $\mathbf{p} = \hbar\mathbf{k}$ for a photon with wave vector $\mathbf{k}$, where $|\mathbf{k}| = 2\pi/\lambda$, if the spectral width $\Delta\lambda$ is small, then Δk is small, and the main contribution to the uncertainty in momentum is due to uncertainty in θ. For small angles, $|\Delta\mathbf{p}| = \hbar k\Delta\theta$, so the inequality relation in equation 6.6 can be expressed as:

$$\Delta x\hbar k\Delta\theta \geq \frac{\hbar}{2}$$

$$\Delta x\hbar\frac{2\pi}{\lambda}\Delta\theta \geq \frac{\hbar}{2} \tag{2.7-1-3}$$

$$\Delta x\Delta\theta \geq \frac{\lambda}{4\pi}$$

This gives the limiting relationship

$$d \cdot \theta = \frac{\lambda}{2\pi} \tag{2.8}$$

which describes the smallest source size d that can be resolved with a finite wavelength λ. This can also be expressed as a coherence length, $L_{coh} = z\theta$, where z is the distance of wavefront from source:

$$L_{coh} = \frac{z\lambda}{2\pi d} \tag{2.9}$$

This relationship also applies in the case of a Gaussian beam laser in the TEM_{00} mode.

Temporal, or longitudinal, coherence is a measure of the correlation between the phases of a wave at any pair of times, such as an initial time t and after a time delay of τ. At a delay of $\tau = 0$, the degree of coherence is perfect, and the distance at which the wave is completely out of phase is the coherence length, L_{coh}, and corresponding time delay referred to as the coherence time, $\tau = \tau_{coh}$. For a light source, temporal coherence describes how monochrome the source is. For example, take a laser with bandwidth $\delta\lambda$ centred about wavelength λ. At $t = 0$ there is no phase difference between different wavelengths. As the time delay increases, such that $t \neq 0$, phase differences accumulate between the different wavelengths. For the waves with wavelength λ and $\lambda + \delta\lambda$, they are exactly out of phase after $\frac{\lambda/2}{\delta\lambda} = \frac{\lambda}{2\delta\lambda}$ wavelengths. This can be expressed as:

$$L_{coh} = \frac{\lambda}{2\delta\lambda}\lambda = \frac{\lambda^2}{2\delta\lambda} \tag{2.10}$$

The coherence time, τ_{coh}, can be expressed as:

$$\tau_{coh} = \frac{L_{coh}}{c} \tag{2.11}$$

In the context of imaging with coherent sources, there is a practical limitation that if the sample scatters the beam at large angles, there may be a significant path difference and associated time delay. The coherence time must be sufficiently long for interference between to take place between the scattered waves so that the resulting diffraction pattern can be collected.

2.5 Oversampling and support constraints

In 1952 Sayre [19] proposed that in principle the phase information can be recovered from the diffraction intensities if they are sampled densely enough, based on the Nyquist-Shannon sampling theorem that states that the phase of a signal can be retrieved if it is sampled at twice the Nyquist frequency [20], [21]. If the phase problem is considered as a set of equations, there would be N equations in both the object and Fourier plane for a CCD with N number of pixels. Since every position is characterised by an amplitude and phase, there is a total of 2N unknowns (N amplitudes and N phases) and only N number of knowns due to the phase problem. However, if the diffraction pattern is sampled at twice the Nyquist frequency, there would be 2N known amplitudes, and in principle the phase can be retrieved. A method to implement this is to add a zero-density region around the object – a region where the amplitude and phase are both known to be zero. If this zero-density region helps increase the dimensions of an N by N pixels object to 2N by 2N pixels, then the oversampling requirement will be fulfilled. Bates [22] also stated that the minimum sampling frequency for the scatter pattern of a non-periodic object necessary to retrieve the phase is twice the Nyquist sampling rate in each dimension. This corresponds to an oversampling factor of 4 in 2D and 8 in 3D, though this has also been countered by Miao and in practice, it is generally accepted that an oversampling ratio of 5 is suitable for use with real data [23].

Despite the proposal that oversampling diffraction patterns provides a solution to the phase problem, support constraints have been key in enabling effective phase-retrieval. The first phase retrieval algorithms were error reduction (ER) algorithms, developed by Gerchburg and Saxton in 1972 [24]. The ER algorithm is based on applying the Fourier transform of the data in the plane of detection – usually referred to as the Fourier plane – to the object plane and back, and applies a set of constraints for both the reconstructed image and reconstructed diffraction pattern after each iteration. Initially, the square root of the measured intensity is taken to be the amplitude of the electric field, and a set of random phases is used to provide an initial guess of the electric field in the Fourier plane. Applying the inverse Fourier transform to this initial guess provides a solution for the exit wave field (EWF) at the object plane. At this point, a support constraint is applied in the object plane. This dictates that the solution must exist within a predetermined area – the support – and the value of the solution must be zero outside this area. The constrained EWF is then projected back into the detector plane by a Fourier transform. The constraint applied here is the modulus constraint, which enforces that the amplitude of the reconstructed data must take the experimentally recorded data. This concludes the first cycle of iteration, and as consecutive iterations are applied, the algorithm may converge to a solution.

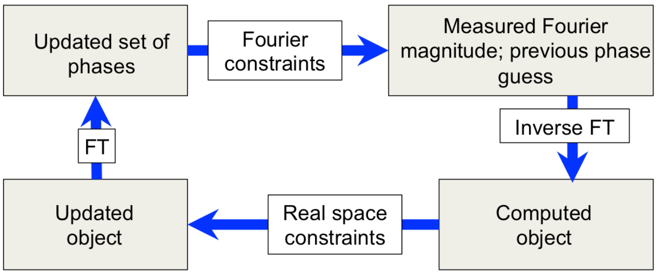

FIGURE 7: Schematic showing an iteration of a typical phase retrieval algorithm for CDI. The measured diffraction pattern provides intensity data, of which the square root is the magnitude in the Fourier plane. The inverse Fourier transform (FT) projects the magnitude in the Fourier plane and the phases from previous iterations on to the object plane, giving a computed object. Real space constraints, such as a support constraint, are applied, giving an updated set of phases and magnitudes. This updated object is projected onto the Fourier plane and the updated phases replace the previous guess, while the measured Fourier magnitude acts as constraints in the Fourier plane.

The ER algorithm is one of the simplest examples of 'alternating projection' (AP) type strategies. Many variations of this strategy have been developed to improve its performance. For example, the Hybrid Input-Output (HIO) method developed by Fienup [25] adjusted the support constraints used during each iteration based on information from a previous iteration in order to prevent stagnation at a local minimum upon convergence. Fienup also proposed using a changing support throughout the algorithm in order to prevent reconstruction of the image rotated by 180 degrees, which has a scatter pattern with the same Fourier modulus as the image in the right orientation. Marchesini et al [26] also proposed a method that reduced the size of the support continually throughout the algorithm.

2.6 Ptychography reconstruction algorithms

Two well-known reconstruction algorithms for ptychography are the extended ptychographic iterative engine (ePIE), and difference map algorithms (DM). These are examples of alternating projection-based algorithms. More recently, Michal Odstrcil developed the orthogonal probe relaxation ptychography (OPRP) error correction technique, and the reconstructions of all images in this project have been performed by Michal using OPRP in combination with ePIE. These methods are described briefly below.

The ePIE algorithm is an improvement on the ptychographic iterative engine (PIE) algorithm, which was the first algorithm to successfully reconstruct an object by ptychography [27], [28]. The ePIE algorithm allowed reconstruction of both the object and probe from the same dataset. In the ePIE algorithm, the scatter pattern is initially assumed to be equal to the Fourier transform of the square of the EWF. An initial guess for the probe is also used – in the PIE algorithm, this initial guess for the probe remained the same throughout the reconstruction process; in ePIE this is updated after each iteration.

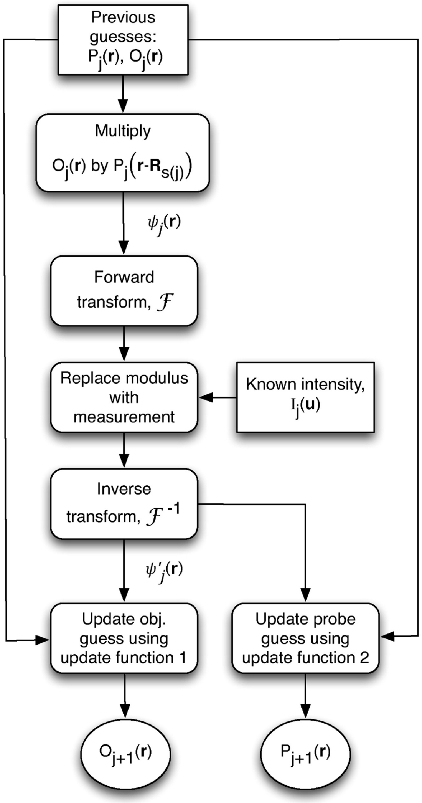

FIGURE 8: Figure from [29]. Flowchart shows the progression of the ePIE algorithm. $\boldsymbol{P_j}(\boldsymbol{r})$ denotes the probe wave field and $\boldsymbol{O_j}(\boldsymbol{r})$ denotes the object; $\boldsymbol{I_i}(\boldsymbol{u})$ is the measured scatter intensity.

The difference map (DM) method is a ptychography algorithm proposed by Veit Elser [20]. In the DM algorithm, the real space (object) and Fourier space constraints are treated as constraint sets and the measured data is to be projected onto both sets. For a point projected onto both constraint sets, the difference between the projections onto each constraint set is used to update the algorithm. This is similar to the HIO method, where the support constraint would be used for the object constraint. In ptychography reconstructions, the overlap constraint is typically used as the real space constraint instead. The DM approach computes all of the exit-waves associated with each scan position in a parallel process such that in each iteration it is a set of exit-waves that are updated, then the probe and object is deconvolved from the set of updated exit-waves.

The orthogonal probe relaxation ptychography (OPRP) method was developed to combat the negative effect of beam instability during a ptychography scan. In the OPRP method, the overlap constraint in real space is relaxed in order to allow slight variations in the illuminating probe in each scan position. This done by approximating small beam movements as a coherent sum of multiple orthogonal modes, using singular value decomposition. In contrast to conventional ptychography reconstruction methods where the value for the probe is an average over many variations, in the OPRP method an individual probe is reconstructed for each scanning position, and observing how the probe changes over the course of the scan can give insight into the temporal instability of the beam. A key advantage that OPRP gives is that the effect of instabilities, caused by the beam or translation stages, in the reconstruction process only shows in terms of the probe illumination, leaving the reconstruction of the object sharp and with little artefacts.

Chapter 3

High Harmonic Generation

In this project, neuron samples are imaged via ptychography with coherent 29 nm radiation, a wavelength that falls within the extreme ultraviolet (EUV) spectrum. High-harmonic generation is used to generate EUV. High harmonic generation (HHG) is a non-linear process that produces spatially and temporally coherent light at extreme ultraviolet (EUV) wavelengths. Incident light drives electrons in an optical medium into oscillation, which creates a dipole moment in the material's atoms – this is given by equation 3.1 which describes the polarisation, P, in terms of susceptibility of the material, χ, and incident field, E:

$$P = \epsilon_0(\chi_1 E + \chi_2 E^2 + \chi_3 E^3 + \cdots) \tag{3.1}$$

In second harmonic generation (SHG), where the material is non-centrosymmetric and its susceptibility approximated by Taylor's expansion to the χ^2 term, the output beam contains radiation of twice the fundamental frequency of the input laser (expressed as a sine wave):

$$\begin{aligned} P &= \epsilon_0(\chi_1 E + \chi_2 E^2) \\ &= \epsilon_0 \chi E_0 cos\omega t \\ &= \epsilon_0 \chi_1 E_0 cos\omega t + \epsilon_0 \chi_2 E_0^2 cos^2\omega t \\ &= \epsilon_0 \chi E_0 cos\omega t + \frac{\epsilon_0 \chi_2 E_0^2}{2} - \frac{1}{2}\epsilon_0 \chi_2 E_0^2 cos2\omega t \end{aligned} \tag{3.2}$$

HHG is an extreme example of this effect, where the interaction between laser photons and atoms is highly non-linear and can no longer be treated as a perturbation modelled by polynomial expansion. Instead, a semi-classical or quantum model can better describe and predict spectral properties of HHG.

3.1 Three-step model

A semi-classical model, the Three-Step Model, first introduced by Corkum et al [31], can be used to describe the generation of radiation from the interaction of an intense laser field and an atomIonisation of the atom due to interaction with intense laser field.

1. Propagation in continuum as the freed electron is accelerated in the laser's electric field.
2. Recombination of electron with parent ion, causing emission of a high-energy photon.

The intense electric field of the laser distorts the potential well of an electron sufficiently to allow tunnel ionization. The freed electron is then accelerated in the laser's electric field away from the parent ion. The oscillating electric field of the laser can cause the electron to accelerate back towards the parent ion, and cause recombination of the electron and the ion. Upon recombination, a high-energy photon is emitted as the electron falls back to ground state. The photon energy is equal to the sum of the electron's kinetic energy and the ionisation potential.

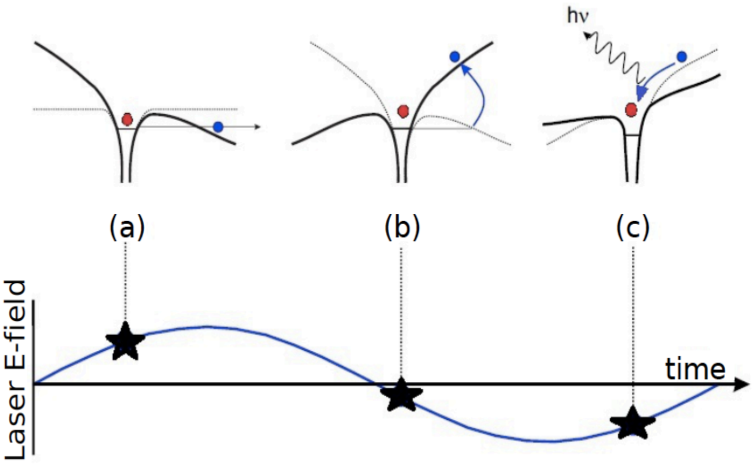

FIGURE 9: Figure taken from [32], showing how the potential well of an electron distorts at different points in the period of the driving laser field. At (a) the electron's potential well is distorted sufficiently for the electron to escape via tunnelling. At (b) the electron is a free particle in the field and its trajectory is affected by the electric field. At (c), the electron recombines with the parent ion, releasing a high harmonic photon.

Though this model uses both classical behaviour (electron and electric field interaction) and quantum behaviour (tunnel ionisation) to describe a complex quantum process, it is particularly useful to consider the dynamics of the free electron after the ionisation step, as this can provide insight into electron behaviour and energy. If a sinusoidal field is assumed for the fundamental laser field, as given in equation 3.3, and the electron assumed to enter the continuum with zero velocity ($at\ t = t_0, where\ \dot{x} = 0\ and\ x = 0$), then the acceleration, velocity, and position of the electron can be derived accordingly by integration:

$$F = eE = eE_0 \cos(\mathrm{\omega t}) = \mathrm{m}_e\ddot{x} \tag{3.3}$$

$$\ddot{x} = \frac{eE_0}{m_e}\cos(\omega t) \tag{3.4}$$

$since\ \dot{x} = 0, x = 0\ when\ t = t_0,$

$$\dot{x} = \frac{eE_0}{m_e}(\sin(\omega t) - \cos(\omega t_0)) \tag{3.5}$$

$$x = \frac{eE_0}{m_e}[\cos(\omega t_0) - \cos(\omega t) + w(t_0 - t)\sin(\omega t_0)] \tag{3.6}$$

It is also useful to consider the energy gained by the electron via Coulomb interaction with the electric field. For a free electron accelerating in a harmonic field E, with angular frequency ω, the time-average kinetic energy gained over one period is known as the ponderomotive energy, U_P, given by:

$$\mathrm{U}_p = \frac{e^2E^2}{4m^2\omega^2} \tag{3.7}$$

The electron trajectory depends on the phase of the laser field when the electron enters the continuum. Figure 10 shows a graph of electric field strength against time, as well as graphs of electron position against time for electrons entering the continuum at different times in the laser period. The laser field changes polarity every half a period, so high harmonics are generated every half-cycle of the laser field. The electron only experiences acceleration towards the parent ion between 0 and $\frac{\pi}{2}$ or π and $\frac{3\pi}{2}$ of the laser period; at all other times the electron experiences acceleration away from the parent ion so no recombination occurs. As such, two spikes in intensity can be observed in the time domain of each oscillation period.

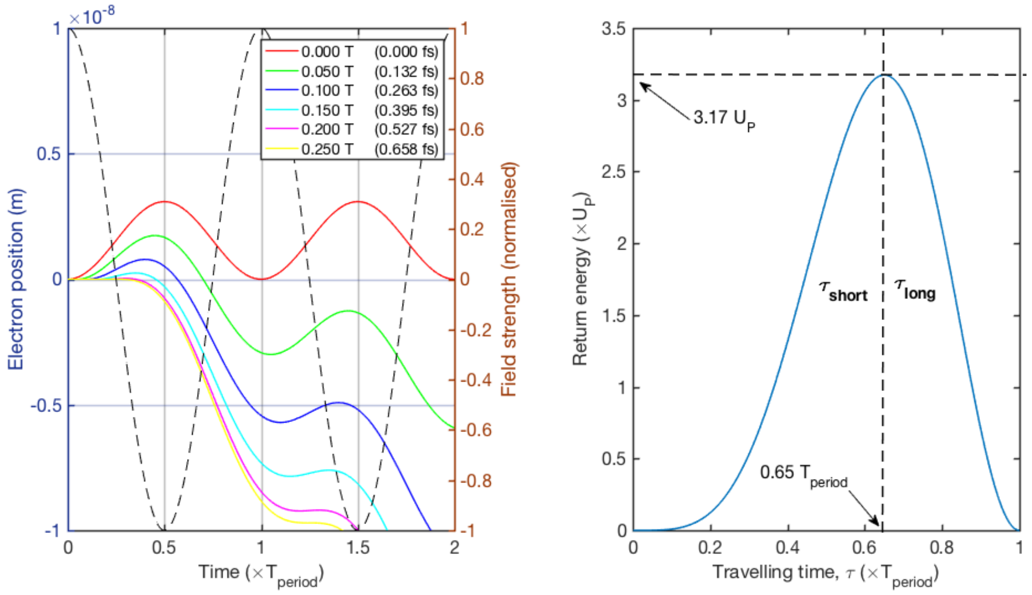

FIGURE 10: Graph of electron position and normalised field strength as a function of period (right); Graph showing return energy of electron at different trajectory times (left). Figure recreated from [3].

For instances of recombination, it is useful to consider the kinetic energy gained by the electron as a function of the time spent in the continuum – its ‘travel time’, given by $\tau = t_1 - t_0$, where t_0 is the release time and t_1 is the return time such that $x(t_1) = x(t_0) = 0$. Substituting into equation 3.6 gives:

$$t_0 = \frac{1}{\omega} arctan \frac{1 - \cos(\omega\tau)}{\omega\tau - \sin(\omega\tau)} \tag{3.8}$$

This expression can be used with equation 3.5 to calculate the kinetic energy of a returning electron as a function of the travel time, τ. This is shown in Figure 10, where the instantaneous kinetic energy of the returning electron is expressed in units of U_P and the travel time is expressed in units of the laser field period, T. Figure 10 shows the maximum kinetic energy – which subsequently gives the cut-off for the highest energy of a photon that can be produced from this process – and two different types of travel times, classed ‘short’ and ‘long’ trajectories, τ_{short} and τ_{long}, create energies lower than the cut-off.

Together with Figure 9, it can be seen that later ionisation times correspond to shorter trajectories, while longer trajectories occur from earlier ionisation times. The harmonic emitted in each case can have the same energy but will have acquired a different relative phase due to a difference in ionisation time and time spent in the continuum – this gives rise to the ‘atomic phase’, discussed further in next section. The maximum from the curve in Figure 10 can be taken directly to give the cut-off energy for an emitted photon [31]:

$$E_{cut-off} = 3.17U_P + I_P \tag{3.9}$$

3.2 Keldysh parameter

The Keldysh parameter compares the ionisation potential of the atom, I_p, to the ponderomotive potiential, U_p (equation 3.7):

$$K = \frac{I_P}{2U_P} \tag{3.10}$$

If K is greater than 1, then the atomic potential dominates the dynamics during laser-atom interaction, and the majority of ionisation events take place via multiphoton absorption. Conversely, if K much smaller than 1, then most atoms would be ionised by quantum tunnelling. HHG often takes place in the tunnelling regime in order to obtain higher flux, as the number of multiphoton absorption events is low and the probability of ionisation via tunnelling is higher.

3.3 Phase matching

In order for efficient emission of coherent radiation, the driving laser field and the generated high harmonic radiation must be in phase. As the driving laser propagates through the generation medium, the harmonic field produced co-propagates with it; the phase velocities of these two fields must be the same in order for the induced harmonic field to build in intensity over the generation region. The contributions from single atoms ionising and emitting at different cycles and positions in the medium must interfere constructively with one another. A schematic showing successful and unsuccessful phase matching is shown in Figure 11, illustrated for the case of phase-matching of radiation generated from second harmonic generation. In Figure 11(a), the harmonic generated at Q is in phase with the harmonic generated at P and so constructively interfere to build up intensity. Conversely, Figure 11(b) shows the case where the harmonic produced at Q is out of phase with the harmonic at P and both waves interfere destructively to cause a reduction in signal of this harmonic.

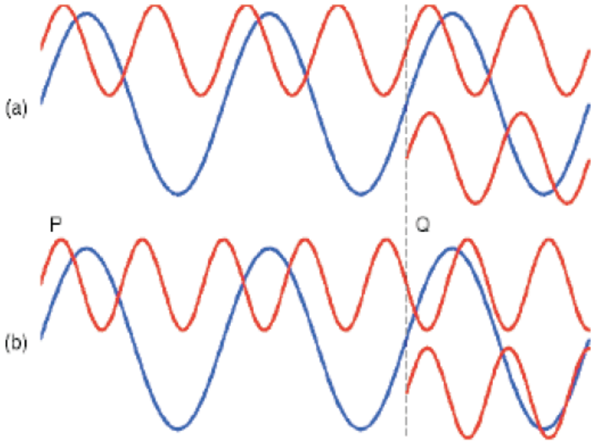

FIGURE 11: Phase matching SHG. In (a), harmonic generated at Q is exactly in phase with the harmonic generated from the start. In contrast, in (b) the harmonic generated at Q is exactly out of phase with the initially generated harmonic. Figure from [33].

Phase-matching is an expression of conservation of momentum, and can be expressed as the phase difference, $\Delta\boldsymbol{k}$, between the qth and fundamental harmonic that needs to be minimised:

$$\Delta\boldsymbol{k} = \boldsymbol{k}_q - q\boldsymbol{k}_f \tag{3.11}$$

where $\boldsymbol{k_q}$ is the wave vector for the high harmonic photon of order q and $\boldsymbol{k_f}$ is the wave vector for the fundamental wave field. For perfect phase-matching, $\Delta\boldsymbol{k} = 0$.

In HHG, phase mismatch is due to and depends on a combination of dispersion, geometric effects, and the atomic phase:

$$\Delta\boldsymbol{k} = \Delta\boldsymbol{k}_{dispersion} + \Delta\boldsymbol{k}_e + \Delta\boldsymbol{k}_{geometric} + \Delta\boldsymbol{k}_{atomic} \tag{3.12}$$

where $\Delta\boldsymbol{k}_{dispersion}$ and $\Delta\boldsymbol{k}_e$ account for dispersion from the neutral gas and free electrons respectively, the $\Delta\boldsymbol{k}_{geometric}$ term accounts for the Gouy phase shift, and $\Delta\boldsymbol{k}_{atomic}$ represents the change in atomic dipole phase.

The atomic phase contribution, $\Delta\boldsymbol{k}_{atomic}$, arises from the delay between electron tunnelling and recombination. It is dependent on the electron's trajectory before recombination and the phase shift that it acquires in the continuum. The atomic phase of the emitted harmonic, ϕ_{at}, is the integral of the quasi-classical action of the electron, $S(t_0, t_1)$, given by:

$$\phi_{at} = \frac{S(t_0, t_1)}{\hbar} + q\omega t_1 \tag{3.13}$$

and $S(t_0, t_1)$ is given by the integral:

$$S(t_0, t_1) = \int_{t_0}^{t_1} \left(\frac{m_e v(t)^2}{2} + I_P \right) dt \tag{3.14}$$

where t_0 and t_1 are the tunnelling and return times of the electron, respectively. The classical action describes the energy of the electron over all points in time spent in the continuum as a function of the kinetic energy, $m_e v(t)^2$. From Figure 9 it can be seen that the majority of the possible return energies can originate from either a long or short trajectory, each of which provide a different phase shift. The resulting contribution to the phase mismatch is [34]:

$$\Delta \boldsymbol{k}_{atomic} = -\nabla \phi_{at} \tag{3.15}$$

The Gouy phase is a phase shift of π that is experienced by a Gaussian beam on passing through a focus, given by:

$$\phi_G(z) = arctan\left(\frac{z}{z_0}\right) \tag{3.16}$$

where z_0 is the Rayleigh length, $\frac{\pi {w_0}^2}{\lambda}$, and z is the propagation distance from the focus. The phase shift acquired as a result of the Gouy phase is given by:

$$\Delta \boldsymbol{k}_{geometric} = q\frac{d\phi_G(z)}{dz} \approx -\frac{qz_0}{z^2 + {z_0}^2} \tag{3.17}$$

This phase mismatch has a dependence on relative position in the z-direction with respect to the focus, and so its contribution to the total phase mismatch changes with z. Consequently, the phase-matching conditions of the system vary through the focus [35].

The effect of dispersion by neutral gas and free electrons on phase matching is an important one, as the HHG process relies on ionisation. Free electrons are produced in all HHG experiments, and during generation, the fundamental and harmonic fields propagate through partially ionised gas. Additionally, the pulsed nature of the laser makes this these two contributions dynamic – all gas atoms are neutral prior to interaction with the laser pulse, but upon interaction there is a fall in percentage of neutral gas species and an increase in amounts of plasma, which eventually plateaus due to saturation of ionisation.

The phase shift from the free electrons can be calculated from the refractive index of plasma, given by:

$$n_e{}^2 = 1 - \frac{\omega_p{}^2}{\omega_0{}^2} \tag{3.18}$$

such that

$$n_e = \sqrt{1 - \frac{\omega_p{}^2}{\omega_0{}^2}} \tag{3.19}$$

where n_e is the plasma refractive index (due to free electrons), ω_0 is the frequency of the fundamental field, and ω_p is the plasma frequency. The latter is a function of the number density of free electrons, N_e:

$$\omega_p = \sqrt{\frac{e^2 N_e}{m_e \epsilon_0}} \tag{3.20}$$

where $N_e = P_\eta N$ depends on the pressure P of generation gas (in atmospheres), the number density of atoms at 1 atm, N, and the fraction of gas ionised, η. Approximating the plasma refractive index given in equation 3.19 to the first two terms using a Taylor's expansion gives $n_e \approx 1 - \frac{\omega_p{}^2}{\omega_0{}^2}$, giving the phase mismatch due to free electrons as:

$$\Delta \boldsymbol{k}_e = -\frac{\pi q \omega_p{}^2}{\lambda_0 \omega_0{}^2} \tag{3.21}$$

The phase mismatch due to dispersion from the neutral and ionised gas can be expressed as:

$$\Delta \boldsymbol{k}_{dispersion} = q k_f \left(n(\lambda_q) - n(\lambda_f) \right) \tag{3.22}$$

$$\Delta \boldsymbol{k}_{dispersion} = \frac{2\pi q P}{\lambda_f} k_f \left(n(\lambda_q) - n(\lambda_f) \right) \tag{3.23}$$

Of the various contributions to phase mismatch, the Gouy phase – with its dependence on the Rayleigh length, which is dependent on wavelength – and the atomic phase dominate at low pressures; at high pressures all terms should be considered.

Chapter 4

Ptychography on EUV beamline

This chapter covers aspects relating to experimental design and set-up. The beamline set-ups for the ptychography experiments are detailed, as well as practical operation and experimental information for ptychography scans. Some practical challenges of the process are also described. A brief description of the specimen preparation process for the neuron samples is also given.

4.1 Laser system

The laser system used for experiments at the University of Southampton consists of a Ti:Sapphire oscillator (Tsunami, Spectra Physics), pumped by a continuous wave Nd:YVO$_4$ continuous wave (CW) laser (Millennia, Spectra Physics), and a regenerative amplifier (Spitfire Pro, Spectra Physics), pumped by a Nd:YLF laser (Evolution, Positive Light).

The CW Millennia is a 3.6 W, 532 nm Nd:YVO$_4$ laser that pumps the Ti:Sapphire oscillator, producing the seed laser. A passive Kerr lens mode-locked cavity is used in the oscillator, with an acoustic-optical modulator (AOM) used to initiate mode-locking. Pulses of 30 fs pulse length and 80 MHz repetition rate are generated in the Ti:Sapphire oscillator, and thee mode-locked laser exiting the oscillator system is observed by a spectrum analyser and optimised for a wide bandwidth (40 nm) centred around 790 nm.

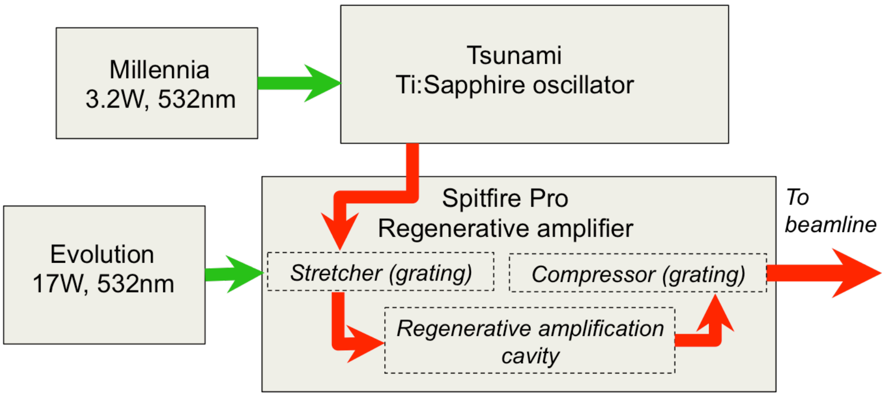

FIGURE 12: Schematic of laser system at University of Southampton; recreated from [3]. The Millennia is a $Nd:YVO_4$ CW laser with an output beam of 532 nm and 3.6 W. The Millennia is a pump laser for the Tsunami, a Ti:Sapphire oscillator. The mode-locked beam from the Tsunami enters the Spitfire Pro, the regenerative amplifier. The Evolution laser pumps the Spitfire with 17 W 523 nm beam from a Nd:YLF laser. Each pulse is first stretched in the CPA amplifier, and then makes 12 round trips in the regenerative amplifier before being recompressed. The overall laser output from the Spitfire is 2.5 W 40-50 fs at a repetition rate of 1 kHz.

Each pulse enters the regenerative amplifier system, where they are first stretched by a grating system as part of the chirped pulse amplification system. The Ti:Sapphire gain medium of the amplifier system is pumped by a 17 W, 1 kHz repetition rate frequency-doubled Nd:YLF laser of 532 nm. Each stretched pulse is switched into the Ti:Sapphire cavity using a Pockels cell and makes 12 round trips in the cavity before exiting via a Pockels cell. Each pulse then passes through a compression grating to give a final output of 40-50 fs pulse length, 2.5mJ per pulse 1 kHz repetition rate pulsed laser beam.

The ptychography imaging experiment was also carried out using the Artemis laser system at the Central Laser Facility at the Rutherford Appleton Laboratories. The Artemis laser system also uses a similar chirped pulse amplification system, though it can achieve much higher power output. The laser is a 30 fs 1 kHz Ti:Sapphire CPA system that operates at a wavelength of 780 nm, and with a maximum output of 12 W. The Artemis laser is also able to generate 13 nm high harmonics with neon gas as the generating medium, though this was not used in the experiments in this thesis.

4.1.1 Mode-locking

The ultrafast laser pulses used in the lab and in the experiments are in the range of 40-60 fs, and this is achieved via a mode-locked laser. Mode-locking methods are key techniques in generating pulses of picosecond and femtosecond durations. In mode-locking, the oscillating modes in a laser cavity are forced to maintain equal frequency spacings such that the phase relation between each mode is fixed, and the modes interfere to produce very short pulses of laser light as output.

4.1.2 Chirped pulse amplification and regenerative amplification

Chirped pulse amplification (CPA) is a technique for amplifying ultrashort laser pulses to peak powers while avoiding detrimental pulse distortion or laser (optic) damage. This is achieved by stretching out the pulse temporally and spatially prior to entering the gain medium, where the pulse can be amplified substantially without encountering intensity-related problems, and then recompressing the pulse after amplification. A pulse stretcher introduces the positive chirp, and an element with opposite dispersion – a compressor – removes the chirp. The stretcher and compressor are often grating pairs.

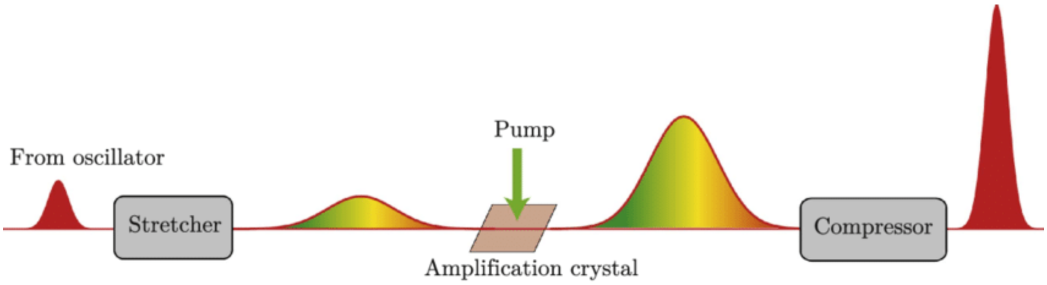

FIGURE 13: Figure from [36]. Schematic showing principle of chirped pulse amplification. In order to avoid damage and non-linear effects during amplification, ultrashort seed pulses from an oscillator are stretched, typically from femtosecond durations to picosecond durations, prior to amplification. The pulse is recompressed afterwards.

The chirped pulse is amplified via regenerative amplification, a process in which multiple passes of the pulse through a gain medium in an optical resonator with an optical switch achieves high amplification. The gain medium is pumped, and a Pockels cell, combined with a polariser, is often used as an optical switch for the resonator. Pockels cells are voltage-controlled wave plates that can rotate the polarisation of a beam that passes through it. They operate based on the linear electro-optic effect (or Pockels effect), in which the change in refractive index of non-centrosymmetric crystalline solids is linearly proportional to the electric field. A pulse is switched into the cavity through a Pockels cells, and can be trapped in the cavity such that it undergoes many round trips and is amplified to a high energy level before exiting the cavity through a Pockels cell.

4.2 Beamline setup for EUV ptychography

Figure 14 shows the experimental design for imaging. A focusing lens of 0.75 m is used to focus the IR beam from the laser system into a gas cell of 3 mm thickness.

Argon (Ar) gas is flowed through the gas cell using a backing pressure of 80 mbar to generate high harmonics. Thin aluminium filters of 200 nm thickness are used to attenuate the IR beam, and the EUV beam is directed onto a curved, focusing MoSi (molybdenum-silicon) multilayer mirror that selects for a single harmonic (29 nm).

Filtering of the IR beam by Al filters is necessary as the conversion efficiency of the high harmonic process is low (approximately 1×10^{-6} [37], [38]) so even after EUV is generated the number of IR photons is an order of magnitude greater than the number of EUV photons. Aluminium provides relatively high transmission for the EUV beam while attenuating the IR beam. The Mo-Si multilayer mirror has a radius of curvature of 40 cm, and has a filtering effect as it reduces the EUV bandwidth and directs the 29 nm EUV beam onto the pinhole aperture. The pinhole is mounted on a stage setup consisting of three Newport linear actuators (LTA series) with 1 μm precision, so minor adjustments to its position can be made when the system is at vacuum. The sample is mounted directly downstream of the pinhole, mounted on a Smaract 3D piezoelectric actuator (SLC-1740) that has nanometer precision. This allows the sample to be shifted in position relative to the pinhole with very high precision. An EUV sensitive Andor DX 424 CCD is used to measure photon flux. The CCD camera is also mounted on a set of three Newport linear actuators such that adjustments can be made to the position of the CCD if necessary.

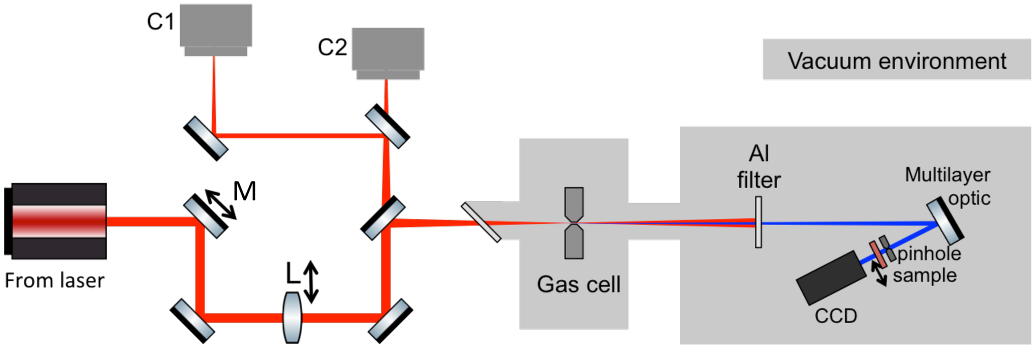

FIGURE 14: Schematic of the beamline setup for ptychography imaging experiments. M is a motorised mirror, L is a motorised lens, and C1 and C2 are cameras (ThorLabs) used for stabilisation. Components within grey background regions are under vacuum environment during the experiment. The lens focuses the beam through an angled vacuum window and into the gas cell. Flowing Ar gas through the gas cell generates EUV. Al filters are used to attenuate the IR beam. The multilayer optic is a curved MoSi multilayer mirror that reduces EUV bandwidth and focuses the beam onto the pinhole. The pinhole and sample are mounted on stages with 3D translation. The beam propagates approximately 6 m from the exit of the laser to the vacuum system. Figure recreated from [3].

The lens and one mirror in the beamline are on a motorised translation stage, and in combination with the stabilisation cameras make up an active stabilisation system that was custom-built for the setup at Southampton by Peter Baksh and Michal Odstrcil. The stabilisation cameras are set up such that the signal measured on camera C1 should directly reflect stability in the gas cell. The accompanying active stabilisation software directs the mirror M and the lens L to make small movements in order to help stabilise the beam.

4.2.1 Use of projection pinhole

The use of a projected pinhole was demonstrated on the Artemis laser beamline while carrying out the ptychography experiment (Figure 15). The experimental geometry is very similar, albeit for the use of an iris upstream of the Al filters that creates a projected pinhole downstream, effectively replacing the need for a physical pinhole.

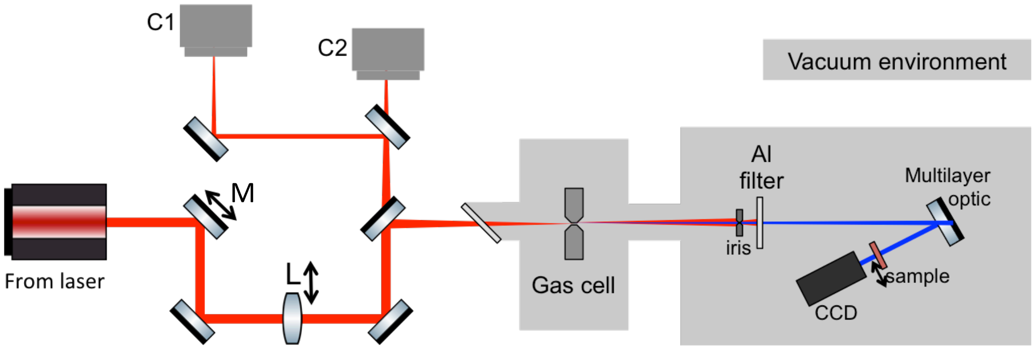

FIGURE 15: Schematic of beamline setup for ptychography experiment using projection pinhole technique. In this setup, there is no physical pinhole used; instead an iris upstream of the Al filters create a projected pinhole

This is the first instance of the application of a projection pinhole to the experiment. It provides the significant advantage of removing the need for a physical pinhole placed in close proximity (50 nm or less) to the sample. A physical pinhole requires fabrication by focused ion beam (FIB) milling in order to achieve sizes of 5-25 nm, and is a delicate component of the beamline.

Aligning both the pinhole and sample – both of which are contained/supported by small aluminium mounts – and positioning them sufficiently close to each other can be challenging in practice. The sample is also scanned relative to the pinhole during ptychography. Both the Si_3N_4 membrane and pinhole can easily sustain damage during alignment or scanning. A projection pinhole is a feasible alternative to using a physical pinhole; the absence of a physical pinhole alleviates some of the alignment challenges and concern for accidentally damaging or destroying the pinhole. The projection pinhole is also constructed using an iris, which is relatively easy to obtain compared to FIB milled pinholes. Placed after generation, it provides the additional benefit of acting like an iris to filter out a portion of the IR beam, which can improve the lifespan of the delicate aluminium filters.

4.3 Experimental operation

As the ptychography setup is under vacuum during experiments, the experiment is operated by commands code that controls all translational stages and operation of the CCD camera, developed by Michal Odstrcil and Peter Baksh.

Several commonly used commands include setting the CCD temperature via Peltier-control, taking exposures with the CCD to monitor the EUV beam, and a raster scan of the pinhole or sample relative to the EUV beam followed by summation of total counts on CCD at each scanning position to generate a low-resolution transmission map (described briefly in Section 4.4).

Another notable feature of the operation code is the 'HDR' (high dynamic range) exposure that was implemented to improve the dynamic range of the experiment. The dynamic range of a CCD refers to how many photoelectrons each pixel of the detector can hold before the accumulation of photoelectrons leak into adjacent pixels. Biological samples can often be poorly scattering and their diffraction patterns only distribute a small proportion of flux into large scattering angles – resulting in a large proportion of flux being recorded in the central region of the CCD detector in the far field. If the pixels oversaturate and signal leaks out to adjacent pixels, the information in all these pixels are rendered useless. The HDR exposure command improves the dynamic range as it forms an image from stitching together consecutive exposures each with decreasing exposure times. The initial exposure is long so that the CCD is allowed to oversaturate – the pixels in the central region of the CCD leak out to adjacent pixels, but pixels at the edge regions of the CCD have sufficient time to detect signal at a higher signal-to-noise ratio. The shorter exposures that follow are enabled by only reading out the central region of the CCD, so information in the central region of the diffraction pattern can be collected without oversaturation of the CCD. An HDR exposure of the pinhole can be seen in Figure 16 (Section 4.4).

4.4 Experimental information

The experimental procedure for ptychography scans starts by aligning the beam path with the sample out of the way, using the IR beam at low power. Coarse alignment can be done while the system is at atmosphere, and once at vacuum and EUV is generated, the EUV beam can be observed via the CCD camera and finer adjustments to alignment made using the translation stages of the pinhole stage and CCD detector. This is necessary to locate and align the pinhole prior to positioning the sample. In the experiments performed at Southampton and the Artemis laser facility a set of pinholes was produced by FIB milling of a 50 nm Si_3N_4 membrane coated with 200 nm Au by Dr Stuart Boden; of these pinholes, the 7μm and 10μm apertures were used for ptychography experiments. To locate the pinholes, the pinhole mount is raster scanned relative to the EUV beam and the signal is recorded on the CCD, the total counts integrated and recorded for each scanning position. This gives a low resolution scanning transmission map of the pinholes, the pinhole mount can be translated to align the selected pinhole in the beam path. A similar raster scan can be done to help align the sample with the beam path. Once the lateral coordinates of the pinhole are known, a similar process can be done where a raster scan in the region of the selected pinhole is performed at each of several positions in the z-direction that the pinhole is moved through – this gives a relatively good estimate for the position of the focus of the EUV beam.

As mentioned in earlier sections, a pinhole upstream of the sample defines a tophat illuminating function; ptychography and reconstruction is more robust when the illuminating function has hard edges as opposed to illumination with weak intensity spreading over a large area. As such it is also ideal to position the pinhole as close to the sample as possible. A USB microscope can be positioned in the vacuum chamber to observe the distance between the pinhole and the sample.

When the pinhole is positioned near the focus of the EUV beam, an HDR exposure of the pinhole shows diffraction rings along the edge of the circular pattern, as seen in Figure 16.

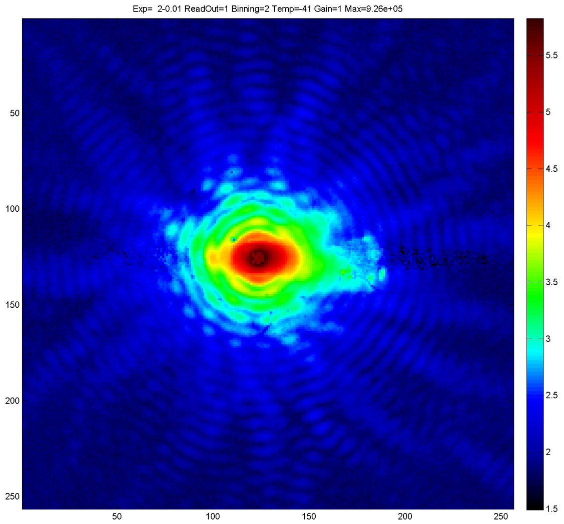

FIGURE 16: An HDR exposure of the pinhole. The HDR exposure process is described in Section 3.3; it increases the dynamic range of the CCD camera by taking multiple diffraction patterns at decreasing exposure times and stitches the images together in order to avoid significant overexposure in the central region of the CCD. Faint black speckles across the centre of the image are a result of the stitching process. The presence of ring patterns is from pinhole diffraction, indicating relatively good coherence in the EUV beam.

Passive stabilisation for the beam was achieved by taping shut all laser and optics enclosures where possible and closing off direct sources of airflow. The active stabilisation system was not used in the experiments presented in this thesis due to equipment issues. As mentioned in Section 2.6, due to the use of OPRP for reconstruction, beam instability manifests more clearly in the reconstruction of the probe illumination than that of the object. In these experiments the reconstructions were able to converge to give relatively clear images.

For the experiment carried out at the Artemis laser facility using the projected pinhole, the iris was 2.2 mm in diameter where it was positioned at the filter plane. The projection of the iris was about 1.75 mm.

4.5 Experimental challenges

During ptychography scans, the CCD detector surface is Peltier-cooled to -50°C, which provides significant noise reduction in data collection. However, a build-up of substance was observed, thought to be oil condensing onto the cold surface of the CCD chip despite vacuum pressures in the low 10^{-5} mbar range. At the end of data collection, raising the temperature of the CCD to ambient temperatures can cause the oil film to coalesce into droplets. The oil may freeze in droplets on the surface if the CCD chip surface is not cleaned before the Peltier-cooling is next used. The layer of oil causes a drop in signal during data collection as the EUV is attenuated and the oil build-up over time can ultimately limit the duration of ptychography scans. The droplet formation between temperature cycles also necessitates frequent removal of the CCD to clean its surface.

The CCD detector surface is cleaned by inverting the CCD and positioning the detector surface over boiling methanol, such that the methanol vapour condenses on the detector surface before gently rolling off, taking any traces of oil with it. As the CCD detector surface and some of its delicate wiring are exposed when cleaning, great care must be taken during the process.

Repeated cleaning of the vacuum chamber surfaces and all components placed in the vacuum chamber was done in order to minimise the amount of oil contaminants present in the chamber. The CCD casing was also removed and several small spots of oil were found on the edges of the casing. These were cleaned, but their origin is unclear. The inner wiring and construction of the CCD could not be cleaned without risking damage to the components themselves, but it was discovered that wrapping the back of the CCD with aluminium foil caused the oil accumulation on the CCD detector surface at -50°C to slow.

Over the duration of this project, multiple vacuum-related issues also arose one after the other. These included sealing and vacuum pump problems. These were eventually remedied, with replacements purchased and installed and repairs done as appropriate.

Chapter 5

Results and Discussion

In this section the reconstructed images of ptychography experiments carried out at Southampton and the Artemis laser facility are presented. Analysis of the data from these reconstructions is also discussed. The analysis largely focuses on δ and β information that can be gained from the reconstruction data, and how can give some insight to composition and material distribution in the imaged neurons.

5.1 Reconstructions of neuron images from EUV ptychography of mouse hippocampal neurons

A sample of 7DIV mouse neurons were imaged using the EUV ptychography setup at the Artemis laser facility and on the beamline at Southampton. These results are presented here. Ptychographic reconstructions for all images presented in this thesis were performed by Michal Odstrcil using the orthogonal probe relaxation (OPRP) technique in combination with the ePIE algorithm.

5.1.1 Ptychography experiments on Artemis beamline

Figure 17 shows the ptychography reconstruction results from one of the experiment performed at the Artemis laser facility. In this experiment, the CCD camera was cooled to -20°C, with a field of view (FOV) of 87 μm.

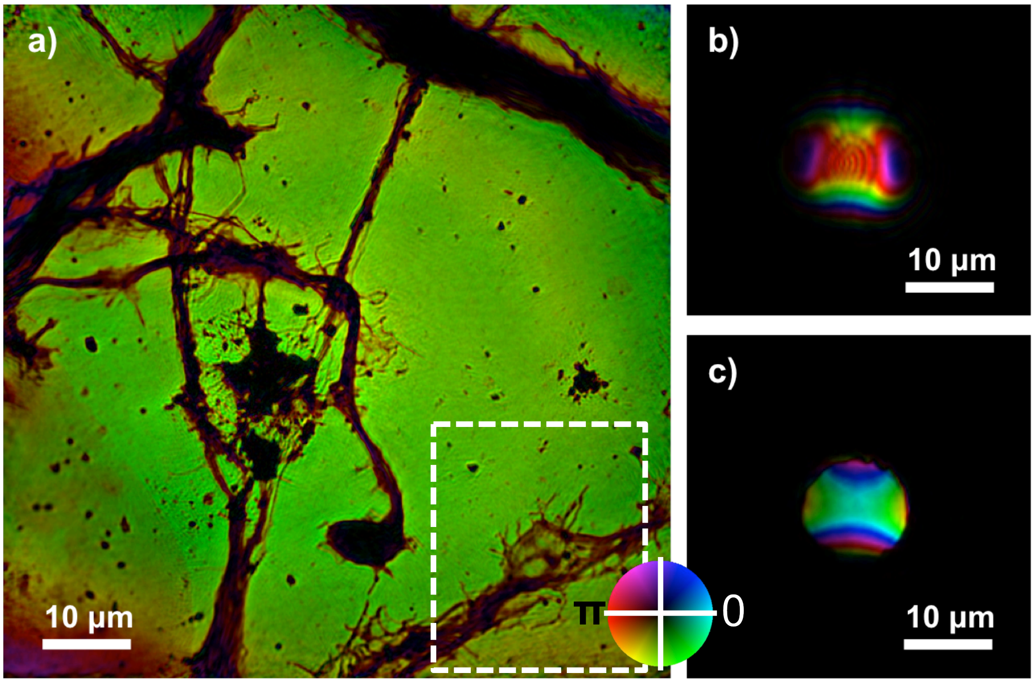

FIGURE 17: (a) Reconstruction in phase and amplitude of 7DIV mouse hippocampal neurons imaged on the Artemis beamline. The pixel size is 134 nm and the field of view is 87 μm. (b) Reconstruction of the probe electric field at sample plane. (c) Reconstruction of probe electric field after back propagation to pinhole plane. Colourwheel shows scale for HSV (hue, saturation, value) representation; the hue represents variation in phase and saturation represents variation in intensity. Region within white dotted line is shown in zoom in view in Figure 18.

Although the image of neurons Figure 17 appears to contain striking features that span the length of the field of view, many of these regions are very dark, indicating low, if any, transmission. This renders much of the information in these dark regions unsuitable for analysis. The thick structures are likely thick bundles of overalapping cells and neurite strands, and it is difficult to distinguish further individual, identifiable neuron structures. However, spindly structures in the bottom right corner of the image within the white dotted-line region appear to be filopodia-like structures that may be consistent with the development of young neurons. Figure 18 shows this region enlarged, and additionally shows this region in the amplitude only and phase only.

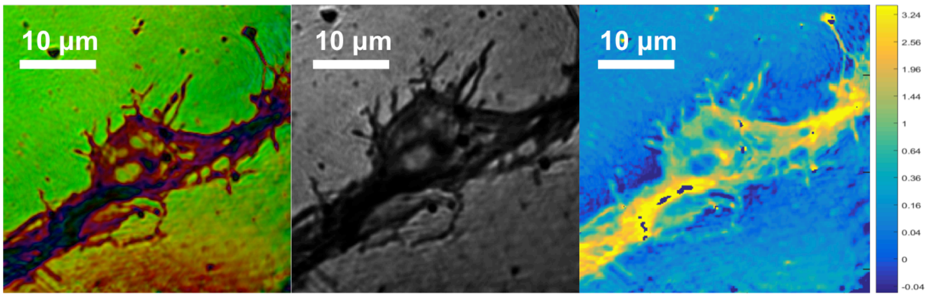

FIGURE 18: Zoom-in views of region within boxed region in Figure 17. Left to right: HSV representation of amplitude and phase; region shown in amplitude only; region shown in phase only.

Figure 19 shows the ptychography reconstruction for the ptychography experiment performed at the Artemis laser facility using a projection pinhole. The CCD camera was cooled to -20°C and the field of view is 46 μm by 48 μm.

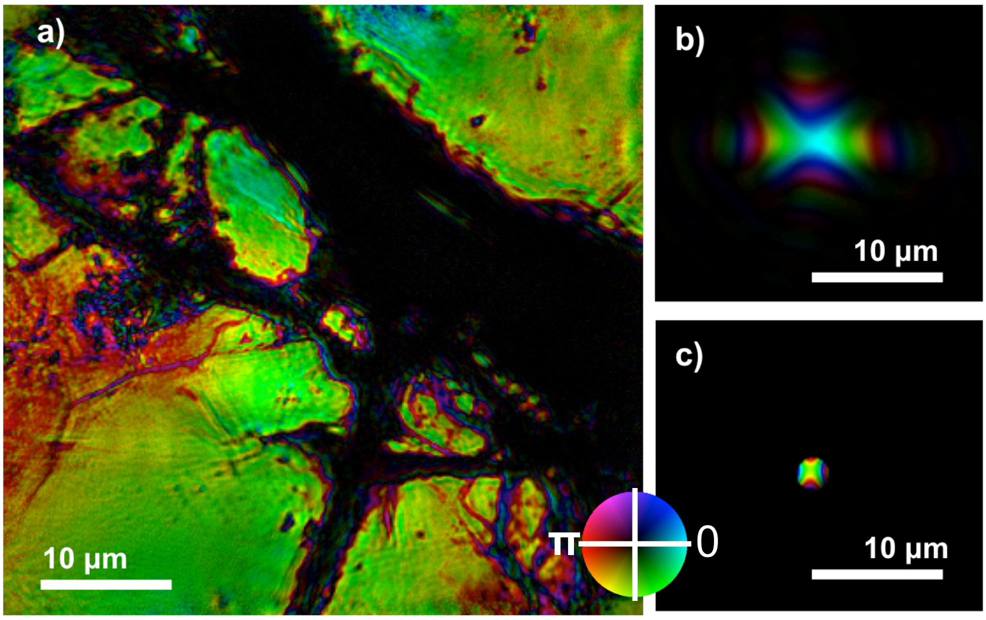

FIGURE 19: Reconstructions of image and probe for 7DIV neuron samples imaged Artemis beamline using projection pinhole technique. The pixel size is 134 nm and the field of view is 46 μm. (a) Reconstruction in phase and amplitude of image. (b) Reconstruction of probe electric field at sample. (c) Reconstruction of probe electric field back propagated to projection pinhole plane.

The reconstruction of this image is noticeably poorer, and this is due to two main reasons: low flux, as well as an illuminating probe that is much more smooth, as compared to the hard edge of a tophat function. This is likely because the projected pinhole is less effective at providing the hard edge than a physical pinhole. Due to the poorer reconstruction quality, this image was not used for extensive compositional analysis in later sections.

5.1.2 Ptychography experiments on Southampton EUV beamline

The 7DIV neuron sample was imaged on the Southampton EUV ptychography beamline following a period of solving equipment issues. In this experiment the field of view is 42 μm.

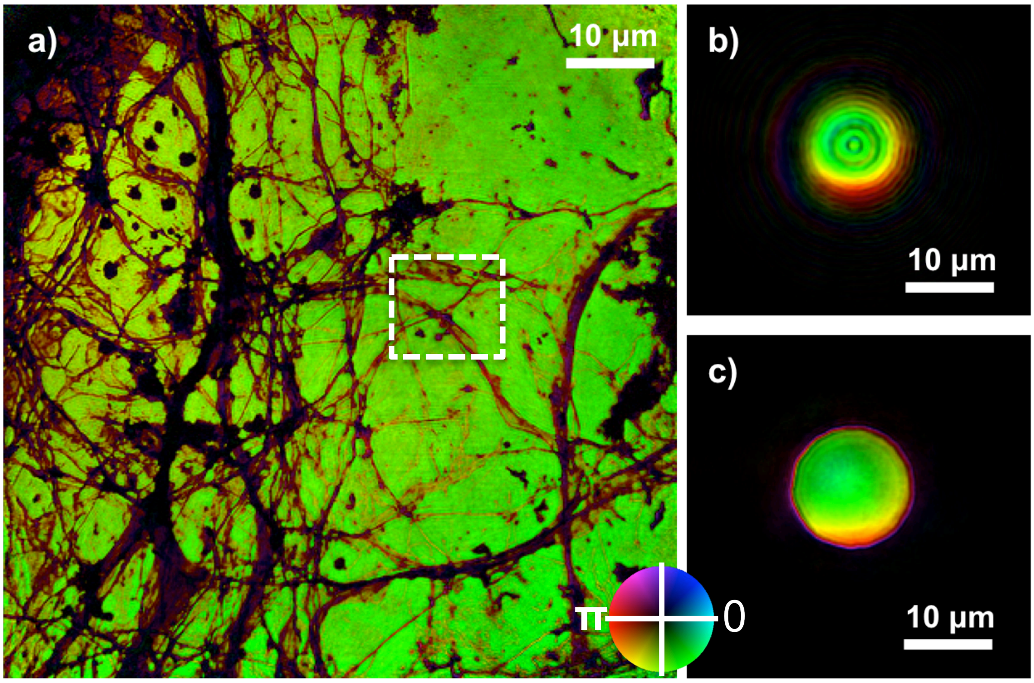

FIGURE 20: (a) Reconstruction in phase and amplitude of 7DIV mouse hippocampal neurons imaged on EUV beamline at Southampton. The pixel size is 102 nm and the field of view is 42 μm. (b) Reconstruction of the probe electric field at sample plane. (c) Reconstruction of probe electric field after back propagation to pinhole plane. Colourwheel shows scale for HSV (hue, saturation, value) representation; the hue represents variation in phase and saturation represents variation in intensity. Region within white dotted line is shown in zoom in view in Figure 21.

In Figure 20, many fine, strand-like structures are seen. These are neuronal processes – small bundles of dendrites and axons. The structures in this image appear clearer as they are more noticeably separated from each other. Importantly, many of the strand-like features are less dark, indicating some transmission through these regions. Figure 21 shows a zoomed in view of the amplitude and phase data of the region within the dotted lines in Figure 20.

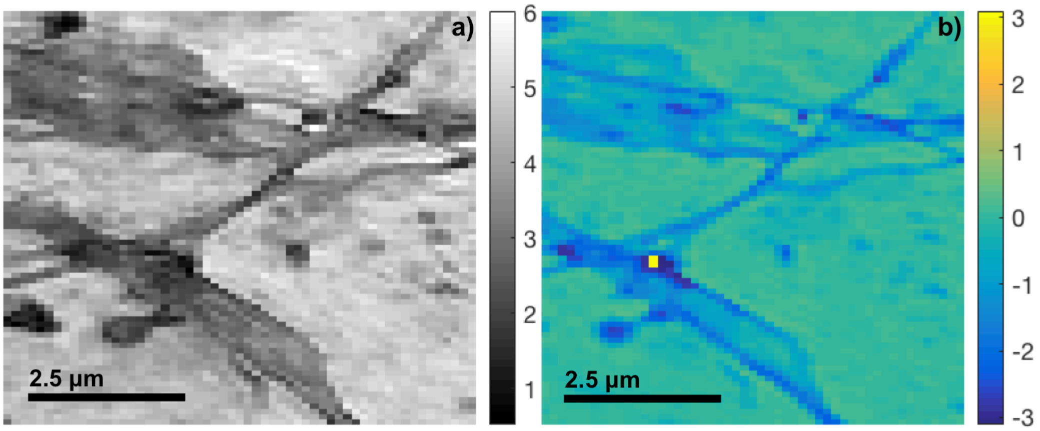

FIGURE 21: Zoom-in views of region within boxed region in Figure 20. Left: region shown in amplitude only; Right: region shown in phase only.

An interesting observation is the difference between how the amplitude and phase look for the same region. From Figure 21, it appears that certain strand-like features are more well-defined in the phase data.

5.1.3 Neuron preparation

The mouse hippocampal neuron samples imaged were prepared by Dr Joanne Bailey at the University of Southampton using the protocol described in this section. The neurons were cultured on silicon nitride (Si_3N_4) membranes of 50 μm thickness. These Si_3N_4 membranes spanned a window of 500μm × 500 μm of a square support. High absorption by at Si_3N_4 at 42 eV (29nm) necessitates that the membrane thickness is minimised for use as a sample support on the EUV beamline.

A summary of the procedure for preparing neuron samples is explained below:

1. The Si_3N_4 substrate is prepared by coating with poly-D-lysine. This creates a layer of charged sites on the substrate, to which the cells can bind, allowing the cells to grow on the surface of the membrane.
2. Hippocampal and cortical neuron cells are extracted from mice embryos. The mouse embryos were dissected and the hippocampal and cortical regions were prepared separately but concurrently. Each region was first treated with a solution of trypsin in excess (0.05% trypsin), which breaks cell-cell connections. The mixture were then homogenised to give a single cell suspensions, and the cells counted.
3. Culture of hippocampal neurons. The culture of the neurons was set up in wells of a six-well plate, with PDL-coated substrates placed in the center of the wells. 1000-2000 hippocampal cells were pipetted onto the membrane surface, while approximately 300,000 cortical cells were pipetted in a ring along the edge of the well. The well was then topped up with culture media – a Neurobasal medium supplemented with B27 and L-glutamine (Glutamax).

The lower density of cells on the substrate is more suited for imaging, while the higher density of cortical cells were used as feeder cells for the growth of the hippocampal neurons by providing growth factors. The neurons were cultivated in 5% CO_2 – providing a pH of 7.4 – at 37°C in the incubator for the desired number of days (days in vivo, DIV).

4. Cell fixation and drying. After the appropriate number of days in culture, the cells were removed from incubation and the culture media removed. Cells were fixed with a solution of 2% paraformaldehyde (PFA) and 20% sucrose in PBS (phosphate buffer saline) for 20 minutes at room temperature. This solution was then washed away and cells were fixed with 100% methanol (ice cold) for 20 minutes. The cells were then slowly dehydrated by consecutive incubations of 5-10 minutes with 70%, then 80%, then 100% ethanol solutions. Lastly, the cells were allowed to air dry.

5.1.4 Neuron structure and feature comparison

Neurons, also known as nerve cells, are the primary components of the nervous system of an organism. They are found in the brain, spinal cord of vertebrate animals, and the peripheral nervous system. They receive, process, and transmit electrical and chemical signals. The typical structure of a neuron, shown in Figure 22, consists of the soma or cell body, dendrites, and axon.

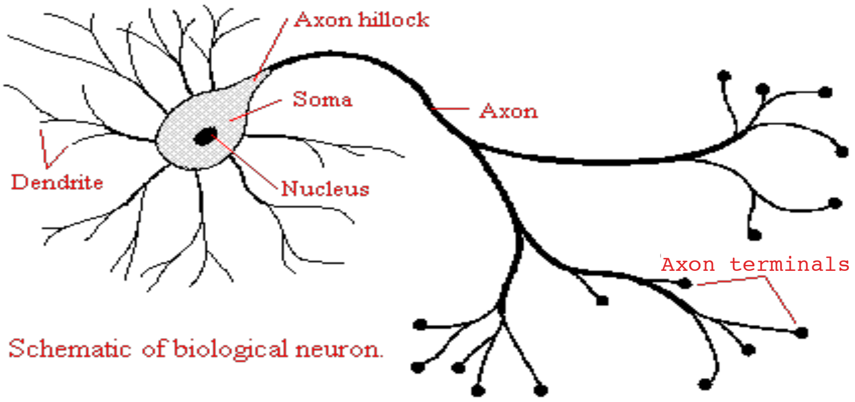

FIGURE 22: A schematic of a neuron showing characteristic structural features including the soma, dendrites, axon, axon hillock from which the axon arises, and axon terminals. Figure from [39].

The nucleus is found in the soma, which is typically compact; dendrites and the axon are filaments that extend from the soma. Dendrites are thin structures that arise from the soma and branch profusely, their furthest branches extending to a few hundred micrometers, giving rise to a complex dendritic network. The axon is a thicker structure that originates at a site called the axon hillock and can extend for great distances and ends by branching into numerous axon terminals (synaptic terminals).

Neurons receive signals via dendrites and send out signals via the axon – an electrical or chemical signal is passed from a neuron to another at a synapse, a junction where an axon terminal is in close proximity to a dendritic spine, allowing a neuronal impulse to be transmitted via chemical neurotransmitters moving across the axon terminal to the dendrite. Dendritic spines are small membranous protrusions from a dendrite; the denrites of a single neuron can contain hundreds to thousands of spines. The axon is typically sheathed by a layer of lipid-rich, electrically insulating myelin, which helps increase the speed at which neuronal impulses travel down the axon without any degradation in signal via a propagation process known as saltatory conduction.

In developing neurons, axons and dendrites are initially neurites – neuronal processes yet to be differentiated– that are decorated with dynamic growth cones at their tips. Growth cones are at the leading edge of these neuronal processes, and they have a round or conical shape with thin, finger-like filopodia as protrusions and flat lamellipodia between them. Neurites at early developmental stages can alternate between growth and retraction as the growth cone reacts to attractive or repulsive guidance cues in the form of chemical gradients or mechanical substrate properties. A major polarity event for a developing neuron is when one of these neuronal processes rapidly grows to become the axon. Following this, the remaining neuronal processes continue their morphological development into dendrites, intracellular transport is polarised, and these lead onto the formation of dendritic spines and synapses. Figure 23 shows a young neuron with developing processes, one of which has begun to grow out faster than the rest, indicating that it will become the axon, while the other processes will become dendrites.

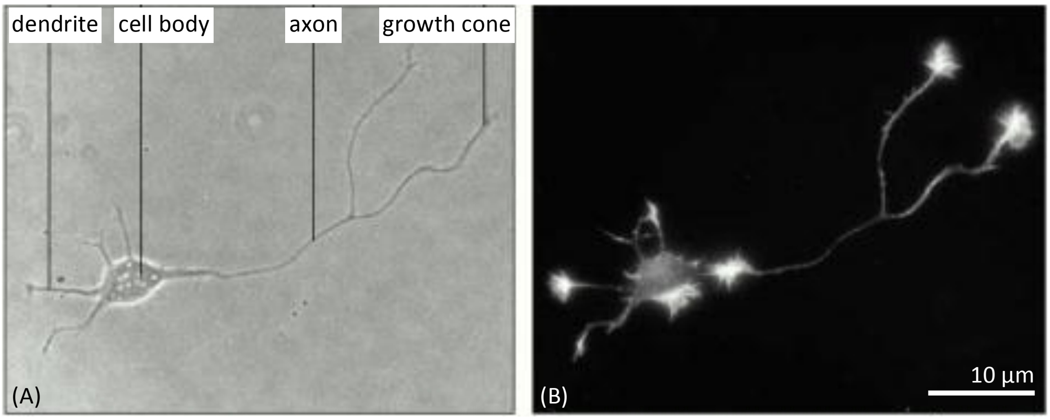

FIGURE 23: A young mammalian neuron with developing processes that have differentiated into the future axon and dendrites. (A) is a phase-contrast picture; (B) is a fluorescent image showing the pattern of staining of fluorescent phalloidin, which binds to filamentous actin. The growth cones can be clearly seen; actin concentrates in the growth cones at the tips of processes that are actively extending and at some other sites of lamellipodial activity. Figure from [40].

Figure 24 below is an optical transmission microscope image of the 7DIV mouse hippocampal neuron sample that was used in the ptychographic imaging experiments, taken before the neuron sample was fixed. Several growth cones and filopodia are highlighted in boxes. The region in highlighted in the coloured box was imaged in the EUV ptychography experiment performed at Artemis. A comparison between the optical microscopy images of the highlighted region before fixing, after fixing and drying, and as imaged via EUV ptychography is shown in Figure 25.

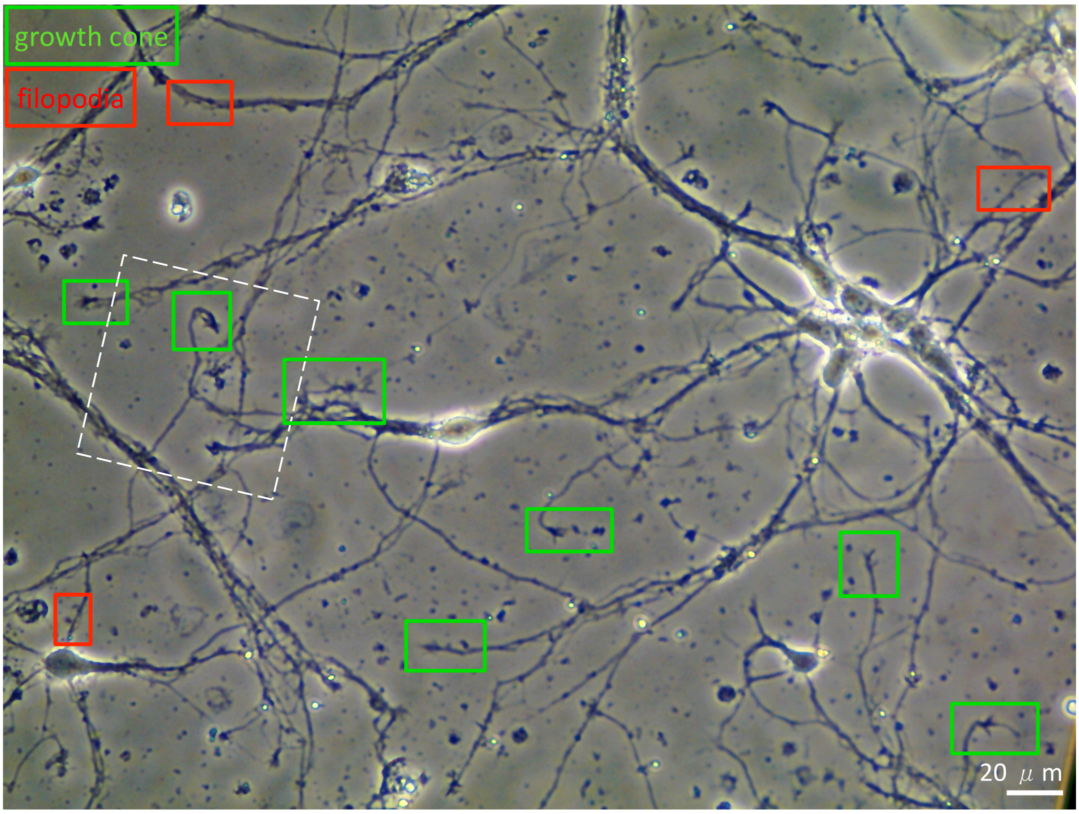

FIGURE 24: Transmission microscopy image of 7DIV mouse hippocampal neurons cultured on SiN membrane that was imaged using EUV ptychography at Artemis. Several growth cones are shown in green boxes; filopodia are shown in red boxes. Region within the white dashed line was imaged in EUV ptychography experiment.

A comparison of the optical microscopy images with the EUV ptychography image demonstrates a significant improvement, with sharper and clearer details and features being discernable in the XUV ptychography image. This is shown in Fig 25.

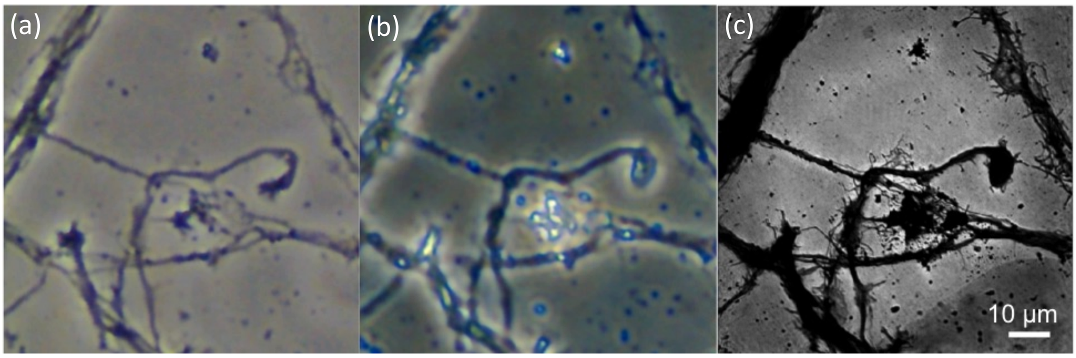

FIGURE 25: Region of 7DIV mouse hippocampal neuron sample imaged by (a) optical microscopy before fixing, (b) optical microscopy after fixing and drying, and (c) EUV ptychography. Images (a) and (b) show a clear loss of finer, delicate structural features after the fixation and drying process. (c) shows a significant improvement by EUV ptychography, with more and clearer fine details and features. EUV ptychography image shown in greyscale for ease of comparison.

Thin features that appear to be filopodia and spines that can be seen in the EUV ptychography image are not resolved in the optical microscope images. Conversely, the larger structures appear as solid regions in the EUV ptychography image – this is because EUV radiation is far less penetrating than visible light, and so much less suited to studying large or thick features than optical microscopy. It should be noted that the fixing and drying process causes the loss of some delicate structure and definition in the neuron features, as can be seen from comparing the optical microscope images of the same region before and after fixing.

5.2 δ/β Analysis

Analysis of the reconstructed image can provide insight regarding sample content and composition. This is afforded by the phase-sensitive nature of ptychography, where phase-retrieval is part of the reconstruction algorithms. Sample thickness calculations may also be possible in certain cases if one should desire.

An overview of the mathematical formulation relating wave field and refractive index, leading to how δ/β can be extracted from the data is presented in Section 5.2.1 below. In Section 5.2.2 an initial analysis was applied to the reconstructions from ptychography experiments at Artemis and Southampton (Figure 18, Figure 20). The initial analysis was a rudimentary method that gave crude but quick analyses of selected regions of interest in the image. A revised analysis was then applied to the 7DIV neuron image reconstructed from the ptychography scan performed at Southampton, as well as a reconstruction of 14DIV neurons imaged previously by Peter Baksh and Michal Odstrcil at Southampton; these are presented in Section 5.2.3.

5.2.1 δ/β for EUV wavelengths

The electric field of beam can be expressed as:

$$E = E_0 e^{iknz} \tag{5.1}$$

where $k = \frac{2\pi}{\lambda}$, $n =$ refractive index of material, and $z =$ distance travelled (ie. sample thickness). For a material with complex refractive index $n = 1 - \delta + i\beta$,

$$E = E_0 e^{ik(1-\delta+i\beta)z}$$

$$E = E_0 e^{ik(1-\delta)z} e^{-k\beta z} \tag{5.2-1-3}$$

$$E = E_0 e^{ikz} e^{-ik\delta z} e^{-k\beta z}$$

where $e^{-ik\delta z}$ is the factor that represents the change in phase (a phase shift, $\Delta\psi$, of $-k\delta z$) and $e^{-k\beta z}$ is the factor that describes the change in amplitude of the original wavefunction, $E_0 e^{iknz}$, on passing through the material. Since intensity, $I \propto |E|^2$,

$$I \propto (E_0)^2 \cdot e^{ik(1-\delta)z} \cdot e^{-ik(1-\delta)z} \cdot (e^{-k\beta z})^2$$

$$I \propto (E_0)^2 \cdot 1 \cdot \left(e^{-k\beta z}\right)^2 \tag{5.3-1-3}$$

$$I \propto {E_0}^2 e^{-2k\beta z}$$

The results of the reconstruction algorithm form a two-dimensional array of complex numbers, each of the form $a + ib$, representing the transmission function through the sample. This data describes the change in intensity or amplitude (via modulus) and a relative phase shift (via argument):

$$transmission\ function \propto e^{-k\beta z} e^{-ik\delta z} \tag{5.4}$$

If the thicknesses of the poly-D-lysine layer and neuron regions are denoted by T_{PDL} and T_{neu} respectively, then:

$$\begin{aligned} &transmission\ function \propto e^{-k\beta T} e^{-ik\delta T} \\ &\qquad = e^{-k\beta_{SiN}T_{SiN}} e^{-ik\delta_{SiN}T_{SiN}} e^{-k\beta_{PDL}T_{PDL}} e^{-ik\delta_{PDL}T_{PDL}} e^{-k\beta_{neu}T_{neu}} e^{-ik\delta_{neu}T_{neu}} \end{aligned} \tag{5.5}$$

and

$$\begin{aligned} &transmission\ function\ of \\ &\qquad background\ region \propto e^{-k\beta_{SiN}T_{SiN}} e^{-ik\delta_{SiN}T_{SiN}} e^{-k\beta_{PDL}T_{PDL}} e^{-ik\delta_{PDL}T_{PDL}} \end{aligned} \tag{5.6}$$

so

$$\Delta\psi = \arg(data) - \arg(background) \tag{5.7}$$

$$T_{neu} = -\frac{(\Delta\psi)\cdot\lambda}{2\pi\delta_{neu}}$$

$$= -\frac{(\arg(\text{data}) - \arg(\text{background}))\cdot\lambda}{2\pi\delta_{neu}} \tag{5.8}$$

and

$$e^{-k\beta_{neu}T_{neu}} = \frac{e^{-k\beta T}}{e^{-k\beta_{SiN}T_{SiN}}e^{-k\beta_{PDL}T_{PDL}}}$$

$$= \frac{|data|}{|background|} \tag{5.9}$$

$$\Delta\mu = \frac{|data|}{|background|} \tag{5.10}$$

$$T_{neu} = -\frac{\lambda}{2\pi\beta_{neu}}\ln(\Delta\mu) = -\frac{\lambda}{2\pi\beta_{neu}}\ln\left(\frac{|data|}{|background|}\right) \tag{5.11}$$

Additionally,

$$\frac{-\left(\Delta\psi - \Delta\psi_{background}\right)}{-\ln(|data|/|background|)} = \frac{2\pi\delta_{neu}T_{neu}/\lambda}{2\pi\beta_{neu}T_{neu}/\lambda} = \frac{\delta_{neu}}{\beta_{neu}} \tag{5.12}$$

Equations 5.7 and 5.10 are initial steps that can be used to process the data directly to obtain the quantities $\Delta\psi$ and $\Delta\mu$. The ratio δ/β can also be calculated very simply from these quantities, using equation 5.12.

Calculating sample thickness is possibility, using equations 5.8 and 5.11, using values of δ and β – which can be calculated for different materials from the CXRO refractive index calculator – for the material of the sample in the target region. δ and β of individual atoms are derived from the atomic scattering factor and number density of the element. For biological samples, it is possible to obtain values of δ and β for a protein using an approximate formula and density for a generic protein [38]. In the case of neuron samples, if the neurons are assumed to be composed entirely of protein, these values of δ and β could be used to calculate neuron thickness. However, it is unlikely that the neuron sample imaged is solely composed of protein, despite being at vacuum imaging conditions.

In practice, the quantities δT, βT, and δ/β may prove to be more useful in analysis. The ratio δ/β is constant and unique for each element or material, independent of density, unlike δ and β. δT and βT can also be calculated relatively easily, and are values which can be obtained solely from the data and do not require the use of approximate or averaged, known values such as material density. From δT and βT, δ/β ratios can be calculated, and the distribution of these values may shed light on compositional distribution in in the biological sample, such as protein or lipid presence and distribution, which may provide biological insight. This is the analysis process used in this project, presented and discussed in the following sections.

5.2.2 Initial analysis

Initially, the analysis process focused on being straightforward to implement manually and was used to generate quick analyses of regions thought to be of interest. In this analysis, a histogram is created from each of the phase data and amplitude data of the selected region for thresholding; these histograms exhibited bimodal distributions, with one peak representing object pixels, and the other representing the background. The width of the object distribution and the value of the background peak were noted. Each pixel was processed such that if it fell outside of the object distribution, the value for the background was itself - hence giving a result of 0 from equations 5.8 and 5.11 – while pixels within the width of the object distribution used the value of the background peak as the background in the equations 5.8 and 5.11. This is a crude way of distinguishing between background regions and object regions, and is not carried over to the revised analysis. However, in the initial stage of studying the reconstructions of the neurons it provided some visual help in distinguishing between background and object when looking at small, zoomed-in regions of the neurons.

A total of eight regions in each image were selected for analysis. These are shown in Figures 26 and 27. Care must be taken in selecting regions for analysis – regions that are both well defined and appear with strong contrast relative to the background may be material or structures that are sufficiently attenuating enough that there is little transmission through the region. The phase data in such regions contain little information.

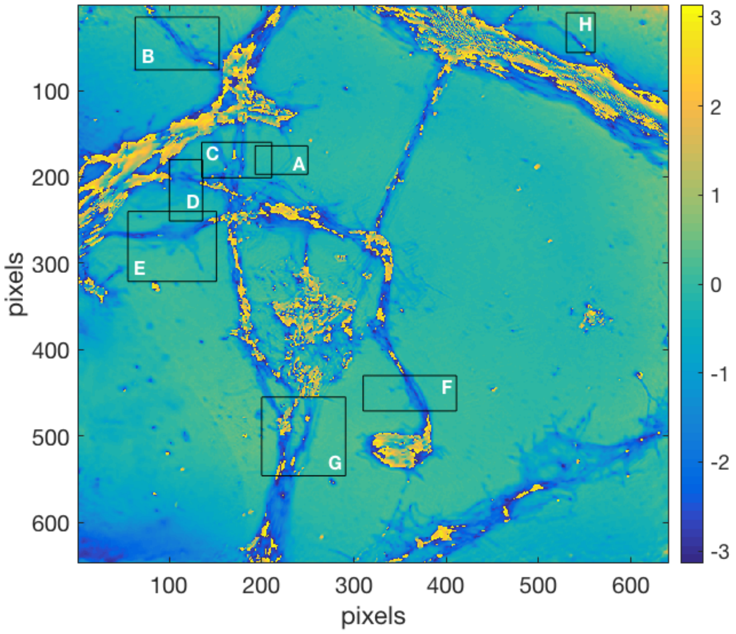

FIGURE 26: Reconstruction of 7DIV neurons imaged at Artemis shown in phase only, with eight regions A–H selected for analysis shown in boxes. The relative phase is given from $-\pi$ to π. Regions of the image in yellow correspond with regions have low transmission, so are mostly left out in analysis. The pixel size for this reconstruction is 134 nm and the field of view is 87 μm.

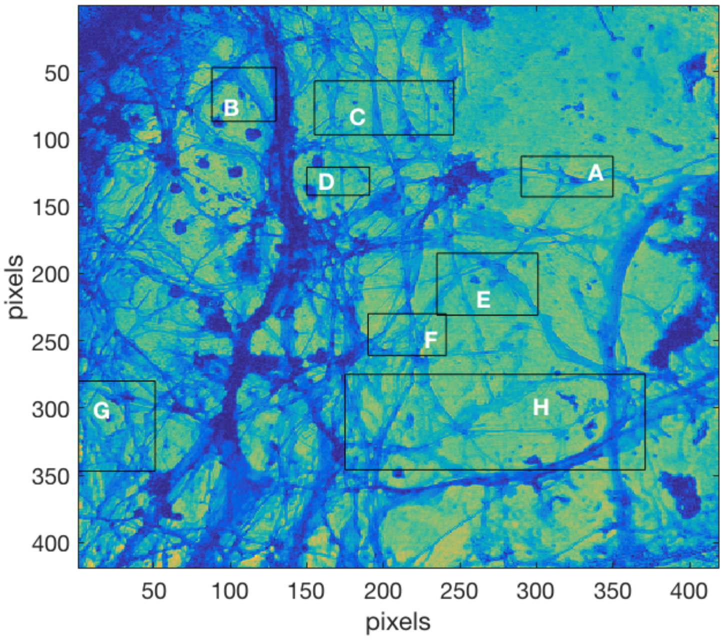

FIGURE 27: Reconstruction of 7DIV neurons imaged at Southampton shown in phase only, with regions selected for analysis, A–H, shown in boxes. The pixel size for this reconstruction is 102 nm and the field of view is 42 μm.

The regions indicated in Figure 26 and 27 were selected for containing fine structures with relatively high transmission through them. Several of the regions also contained interesting features, such as differences in appearance between the plots of amplitude and phase, or web-like regions.

A selection of the analyses for these regions is presented in Figures 28 – 33. In these analyses, histogram analysis of the amplitude and phase data was used to identify a threshold value that would separate signal from background. Though a crude estimate, it was useful for quickly processing the data. For each region, the plots of the amplitude data and phase data are shown, with annotated lines indicating the line profile along which δT and βT are plotted. Finally, a 2D visualisation of δ/β values is shown.

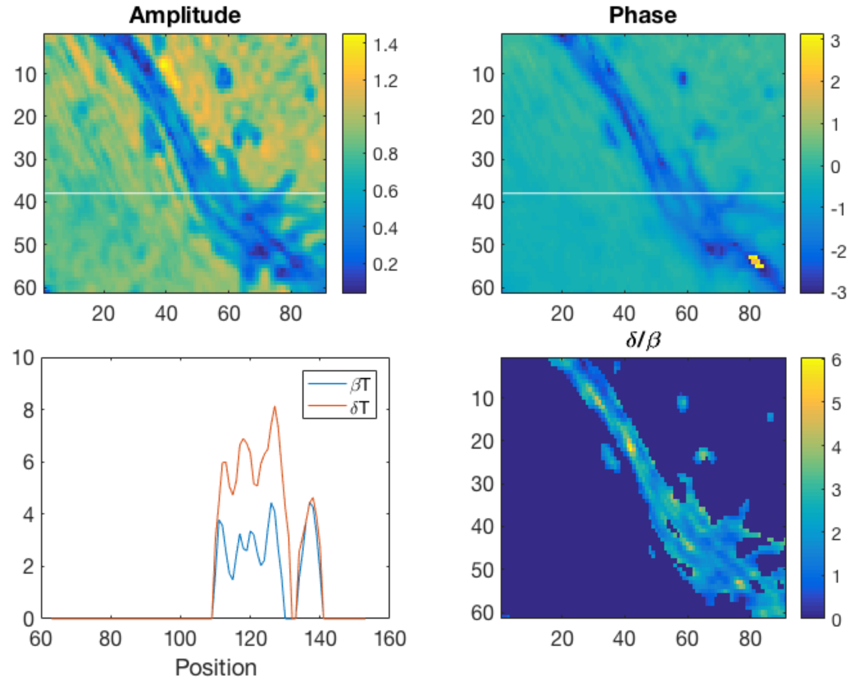

Figure 28: Region B from Figure 26 (7DIV neuron Artemis reconstruction). Clockwise from top left: region B shown in amplitude only with selected line in white; region B shown in phase only with selected line in white; 2D visualisation of δ/β for neuron structure excluding background; plots of δT and βT along line profile indicated. Axes are represent position (pixels; pixel size 134 nm). δT and βT track similarly in shape.

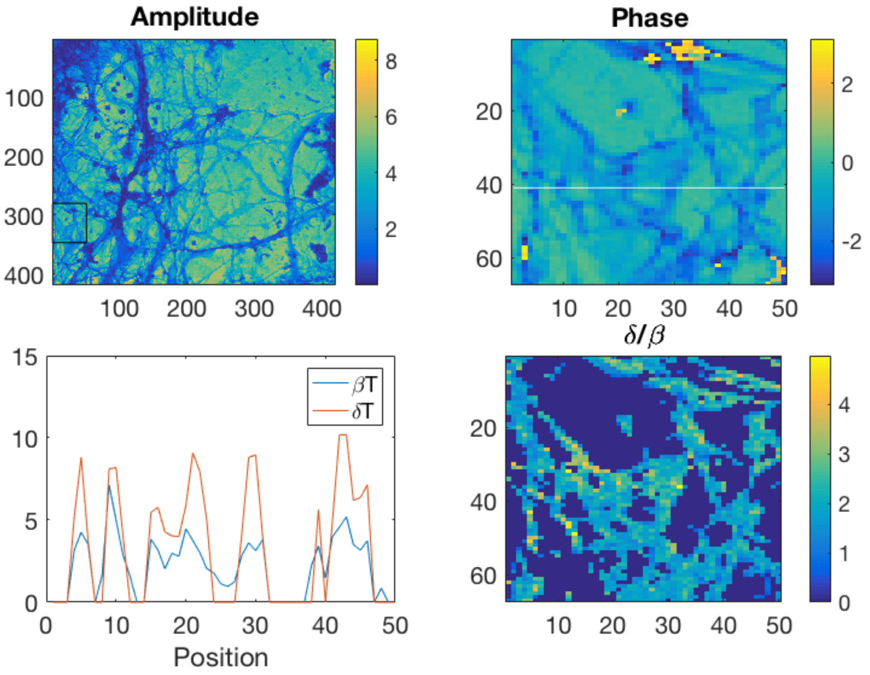

FIGURE 29: Region G from Figure 27 (7DIV neuron Southampton reconstruction). Clockwise from top left: entire reconstruction shown in amplitude only with region G in bottom left of image boxed; region G shown in phase only with selected line in

white; 2D visualisation of δ/β for neuron structure excluding background; plots of δT and βT along line profile indicated. Axes represent position (pixels; pixel size 102 nm). δT and βT track similarly in shape.

In Figures 28 and 29 above it can be seen that both δT and βT plots trace similar graph shapes, demonstrating that δT and βT can track very closely and quite reliably for relatively well-defined features.

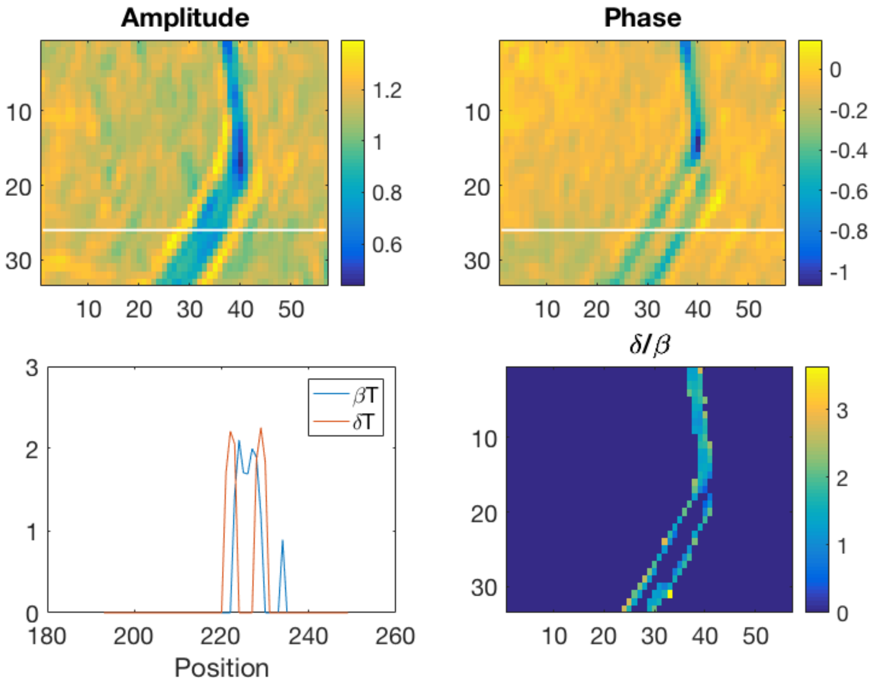

FIGURE 30: Region A from Figure 26 (7DIV neuron Artemis reconstruction). Clockwise from top left: region A shown in amplitude only with selected line in white; region A shown in phase only with selected line in white; 2D visualisation of δ/β for neuron structure excluding background; plots of δT and βT along line profile indicated in amplitude and phase displays. Axes are represent position (pixels; pixel size 134 nm). There is a notable difference between the amplitude and phase visualisation, also seen in the line profile of δT and βT.

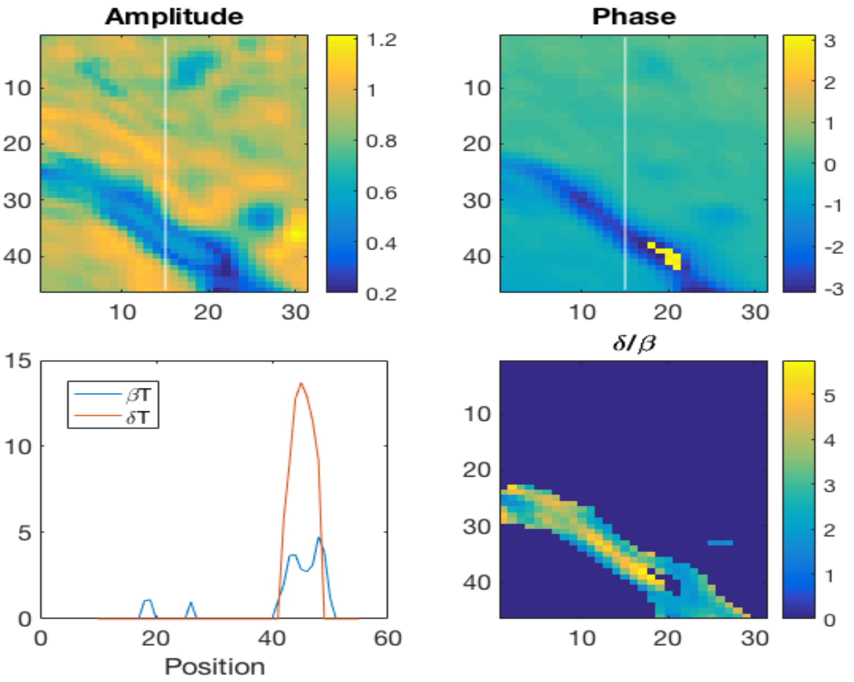

FIGURE 31: Region H from Figure 26 (7DIV neuron Artemis reconstruction). Clockwise from top left: region H shown in amplitude only with selected line in white; region H shown in phase only with selected line in white; 2D visualisation of δ/β for

neuron structure excluding background; plots of δT and βT along line profile indicated in amplitude and phase displays. Axes are represent position (pixels; pixel size 134 nm). There is a significant difference between the phase and amplitude visualisation of the region – the feature looks like 2 strands in the amplitude visualisation and a single strand in the phase visualisation. This is also seen in the line profile of δT and βT.

Figures 30 and 31 show examples of a visible difference between amplitude and phase data, also reflected in a difference in line profiles for δT and βT. These often appear in the form of a feature that appears as two strands in the phase visualisation and a single strand in the amplitude visualisation, or vice versa. A possible reason for this difference may be due to the structure present – there may be a different material on either side of the strand-like structure, which also gives rise to a similar pattern in change of δ/β values.

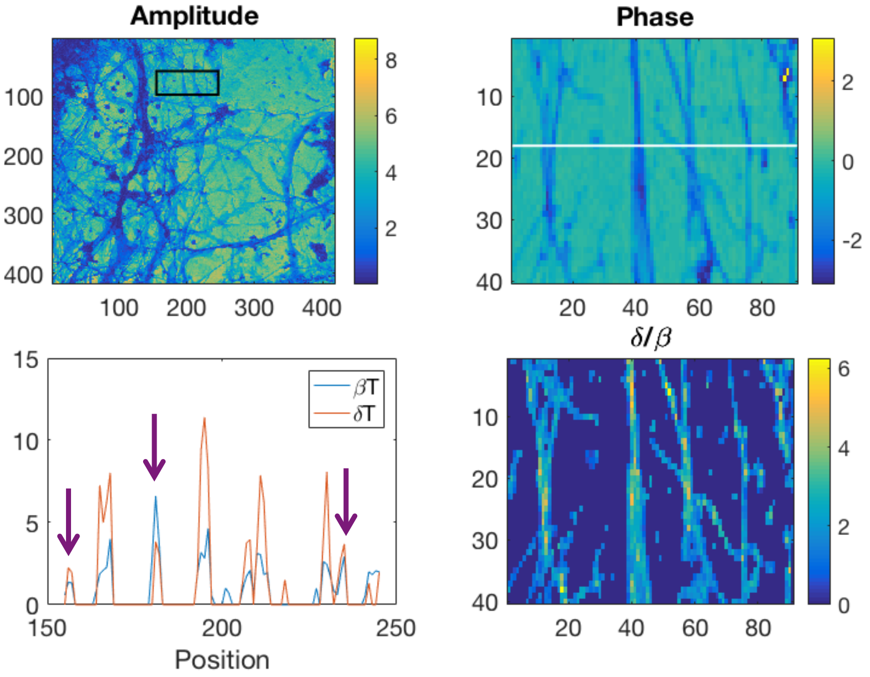

Figure 32: Region C from Figure 27 (7DIV neuron Southampton reconstruction). Clockwise from top left: Whole reconstruction shown in amplitude only with selected region in top of image boxed; region C shown in phase only with selected line in white; 2D visualisation of δ/β for neuron structure excluding background; plots of δT and βT along indicated line profile. Axes are represent position (pixels; pixel size 102 nm). Observing δT and βT for features along the selected line, the δ/β ratio varies but is similar for most features, but the features in the indicated positions (purple arrows) have notably different δ/β ratio (close to 1 or less than 1).

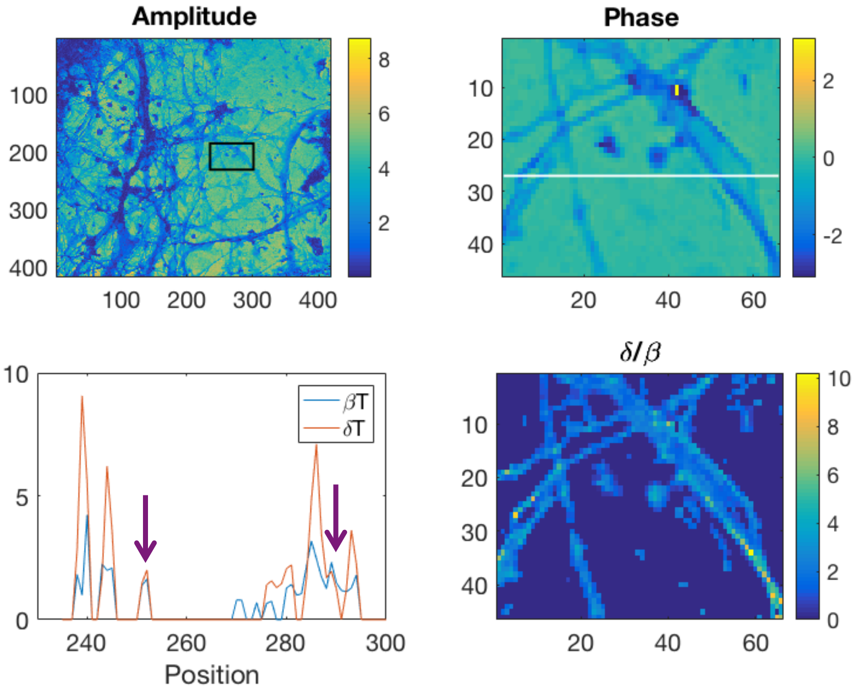

Figure 33: Region E from Figure 27 (7DIV neuron Southampton reconstruction). Clockwise from top left: Whole reconstruction shown in amplitude only with selected region in top of image boxed; region E shown in phase only with selected line in

white; 2D visualisation of δ/β for neuron structure excluding background; plots of δT and βT along indicated line profile. Axes are represent position (pixels; pixel size 102 nm). Observing δT and βT for features along the selected line, the δ/β ratio varies but is similar for most features, but the features in the indicated positions (purple arrows) have notably different δ/β ratio (close to 1 or less than 1).

Figures 32 and 33 show examples where, along a line, the δ/β ratio is mostly similar, but significantly different for some segments. δ/β ratios are typically greater than 1, so cases where δ/β is very close to 1 or less than 1, indicating $\delta < \beta$, stand out. This may indicate a significant change in content between different strands, which poses interesting questions about whether differing composition may have relation to biological structure.

5.2.3 Revised analysis

Initially, the analysis process focused on being straightforward to implement manually and was used to generate quick analyses of regions thought to be of interest. In this analysis, a histogram is created from each of the phase data and amplitude data of the selected region for thresholding; these histograms exhibited bimodal distributions, with one peak representing object pixels, and the other representing the background. The width of the object distribution and the value of the background peak were noted. Each pixel was processed such that if it fell outside of the object distribution, the value for the background was itself - hence giving a result of 0 from equations 5.8 and 5.11 – while pixels within the width of the object distribution used the value of the background peak as the background in the equations 5.8 and 5.11

Following this initial analysis, Dr Bill Brocklesby of the Ultrafast x-ray group developed a MatLab routine for analysis of this nature. In this routine, the phase and the amplitude data is sorted into histograms, but the identification of the peak values and assignment of the peaks – whether representing object pixels or background pixels – is automated. Gaussisan distributions were also fit to the histograms. The peak value of the distribution representing the background was taken to be the average value of the background. δT and βT are then calculated, in the same way as in the initial analysis. The revised analysis routine also had a simple graphic user interface that allowed for region selection. While the revised analysis is much more robust in its processing of the data, care must be taken in applying it. In order to get a robust analysis, the selected region should be relatively small, and more importantly, contain a large background region, so that the histograms of the data show clear, clean distributions. As such, this revised analysis is suited to the analysis of individual features from the reconstruction of the neurons.

In this revised routine, δ/β is not calculated – instead, δT and βT graphs can be generated. This is because there are negative and zero values of δT and βT respectively, which is due to overall noise in the data as a result of the ptychographic reconstruction. If $\beta = 0$, the value of δ/β is undefined, which results in a large fluctuation in δ/β values.

As Figure 26 from the ptychography experiment carried out at the Artemis laser facility has much fewer suitable features to study, analysis using this routine was mainly applied on the reconstruction shown in Figure 27, from the EUV ptychography of 7DIV neurons at Southampton.

It was further applied on the reconstruction results from a previous ptychography experiment carried out by Peter Baksh and Michal Odstrcil in the research group, shown in Figure 34 below, of 14DIV mouse hippocampal neurons.

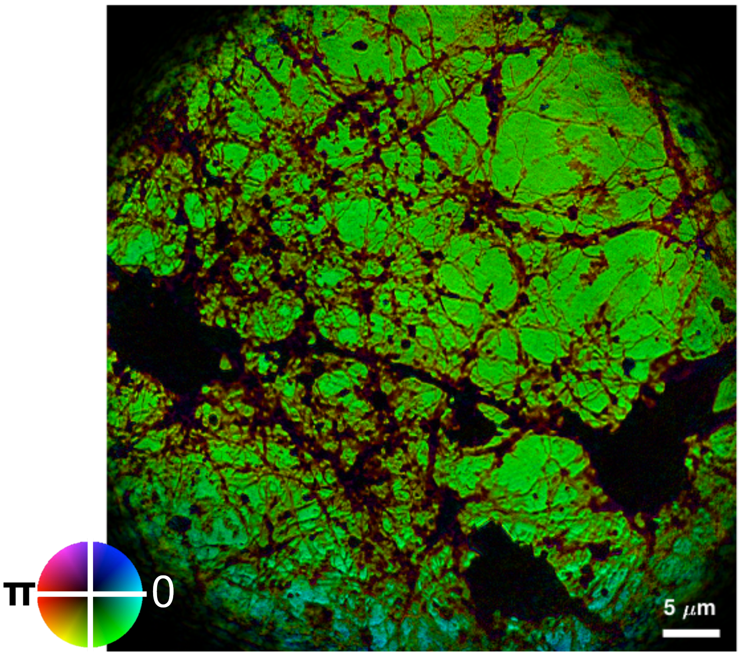

FIGURE 34: Reconstruction in phase and amplitude of 14DIV mouse hippocampal neurons imaged on EUV beamline at Southampton by Peter Baksh and Michal Odstrcil. The pixel size is 42 nm and the field of view is 55 μm.

In these analyses, the δ/β ratio is not computed outright due to large fluctuations in this value if $\beta = 0$. Instead, it is better to consider the graphs of δT and βT to observe any changes in δ/β along the cross-section line. A selection of analyses regions is presented below.

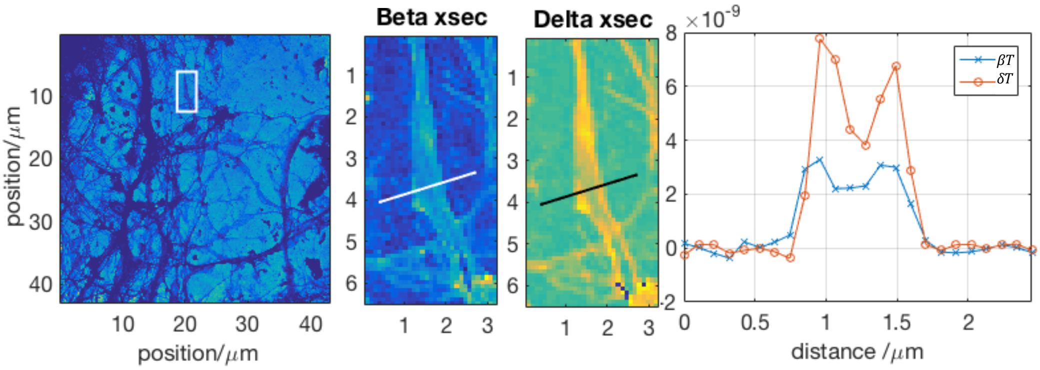

FIGURE 35: Sectional analysis of 7DIV neuron Southampton reconstruction, showing that δT and βT track similarly for a selected feature. Left to right: Full image of the reconstruction in intensity, showing selected region for analysis boxed in white; Beta xsec graph shows selected region in amplitude with selected line segment; Delta xsec graph shows selected region in phase with selected line segment; plot of δT and βT along selected line segment. All axes represent position, given in μm. There are slight differences in clarity of features between the beta xsec and delta xsec graphs.

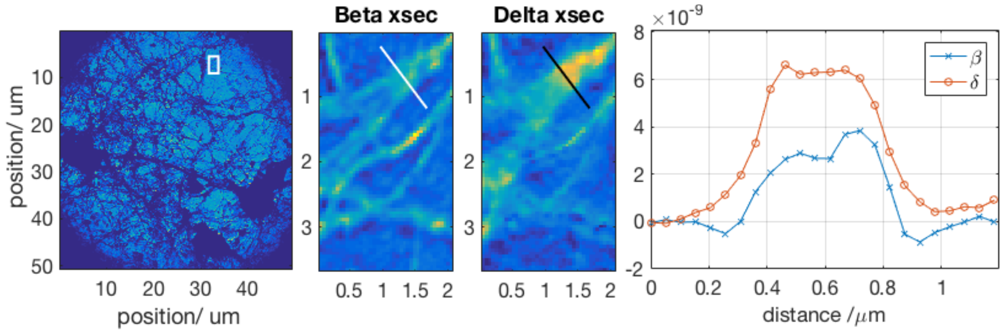

FIGURE 36: Sectional analysis of 14DIV neuron Southampton reconstruction, showing that δT and βT track similarly for a selected feature. Left to right: Full image of the reconstruction in intensity, showing selected region for analysis boxed in white; Beta xsec graph shows selected region in amplitude with selected line segment; Delta xsec graph shows selected region in phase with selected line segment; plot of δT and βT along selected line segment. All axes represent position, given in μm. There are slight but noticeable differences between the variation in magnitude of the amplitude in the beta xsec graph and the phase in delta xsec graph.

Figures 35 and 36 show that δT and βT often tracks similarly for a feature, though the phase and amplitude data may look different – this may be in terms of spatial features, or in magnitude.

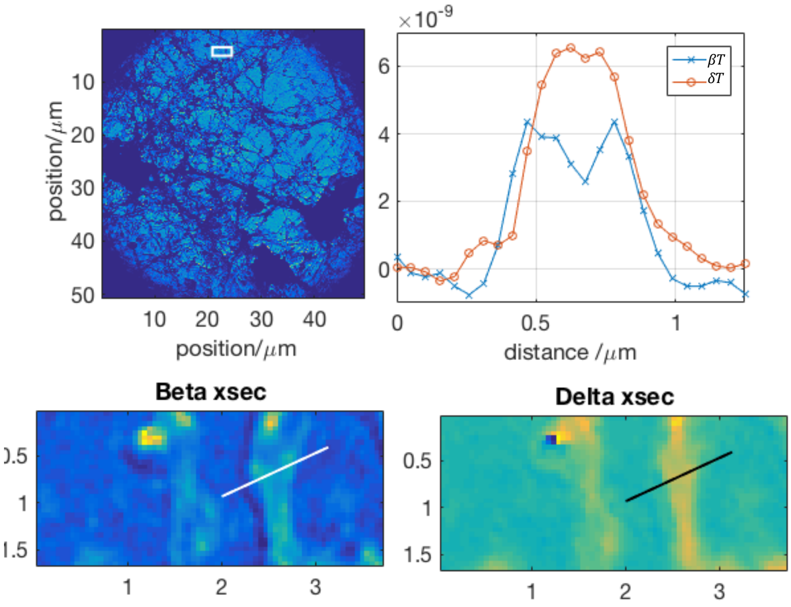

FIGURE 37: Sectional analysis of 14DIV neuron Southampton reconstruction, showing an example where there is a change in δ/β across a feature. Top (left to right): Full image of the reconstruction in intensity, showing selected region for analysis boxed in white; plot of δT and βT along selected line segment. Bottom (left to right): Beta xsec graph shows selected region in amplitude with selected line segment; Delta xsec graph shows selected region in phase with selected line segment. All axes represent position, given in μm. From the graph of δT and βT, it can be observed that the value of δ/β is similar on either edge of the strand, but significantly different in the middle region. This feature is relatively wide.

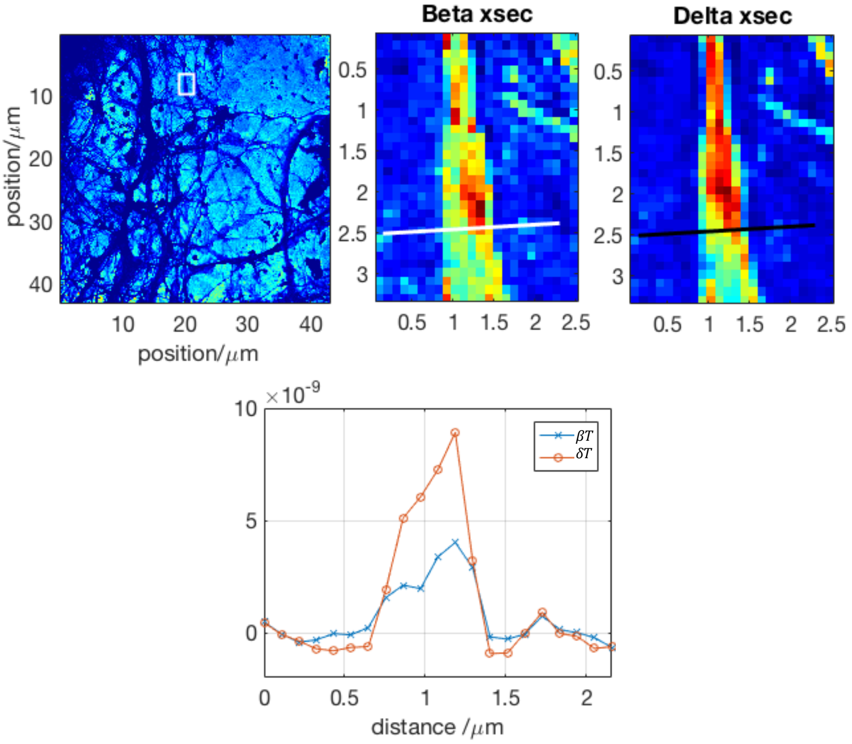

FIGURE 38: Sectional analysis of 7DIV neuron Southampton reconstruction, showing an example where there is a change in δ/β across a feature. Top (left to right): Full image of the reconstruction in intensity, showing selected region for analysis boxed in white; plot of δT and βT along selected line segment. Bottom (left to right): Beta xsec graph shows selected region in amplitude with selected line segment; Delta xsec graph shows selected region in phase with selected line segment. All axes represent position, given in μm. From the graph of δT and βT, it can be observed that the value of δ/β is similar on either edge of the strand, but varies in the middle region. This feature is relatively wide – it may be a thick strand or a bundle of neurites.

Figures 37 and 38 show an interesting situation where there is a change in δ/β across a single structure. This likely indicates a change in material. More importantly, this may be a way to relate compositional distribution and structure. For example, as an initial approximation, neurite strands could be thought of as tubular structures. The tube wall and tube contents may be different materials.

Figures 39 – 41 shown below show examples of unusual δ/β values. δ/β ratios for biological macromolecules such as proteins and lipids are in the range of 1.0–2.0 and 1.7–3.0 respectively. As it is likely that many neurite strands would be composed of a mix of protein and lipid, $\delta/\beta \sim 1$ across an entire strand stands out as different. There are also no notable materials for which $\beta > \delta$, such that $\delta/\beta < 1$, so strands that show such behaviour in δ/β also bear need for further investigation.

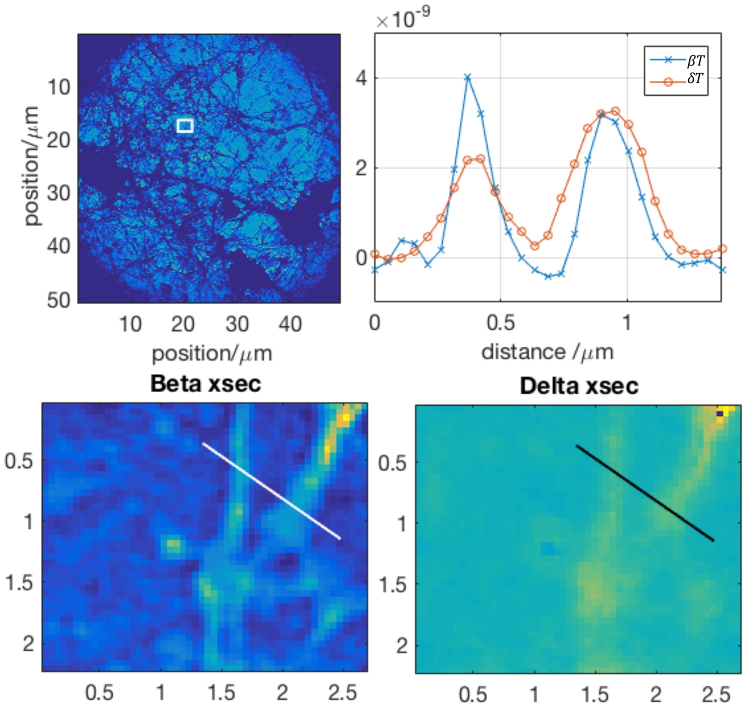

FIGURE 39: Sectional analysis of 14DIV neuron Southampton reconstruction, showing an example where δ/β is significantly different across two features. Top (left to right): Full image of the reconstruction in intensity, showing selected region for analysis boxed in white; plot of δT and βT along selected line segment. Bottom (left to right): Beta xsec graph shows selected region in amplitude with selected line segment; Delta xsec graph shows selected region in phase with selected line segment. All axes represent position, given in μm. From the graph of δT and βT, it can be observed that the value of δ/β is different across two features that look largely similar. Notably, $\delta/\beta \sim 1$ for one feature, whereas $\delta/\beta < 1$ for a different feature.

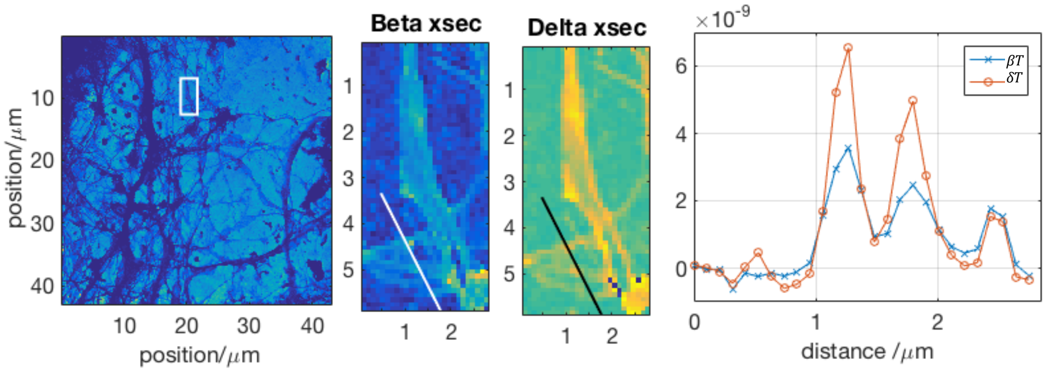

FIGURE 40: Sectional analysis of 7DIV neuron Southampton reconstruction, showing δ/β varying over different features. Left to right: Full image of the reconstruction in intensity, showing selected region for analysis boxed in white; Beta xsec graph shows selected region in amplitude with selected line segment; Delta xsec graph shows selected region in phase with selected line segment; plot of δT and βT along selected line segment. All axes represent position, given in μm. The graph of δT and βT across three separate strand-like features show that two strands have similar δT and βT variation across each strand and $\delta/\beta > 1$, while one strand has a notably different δT and βT variation and $\delta/\beta < 1$.

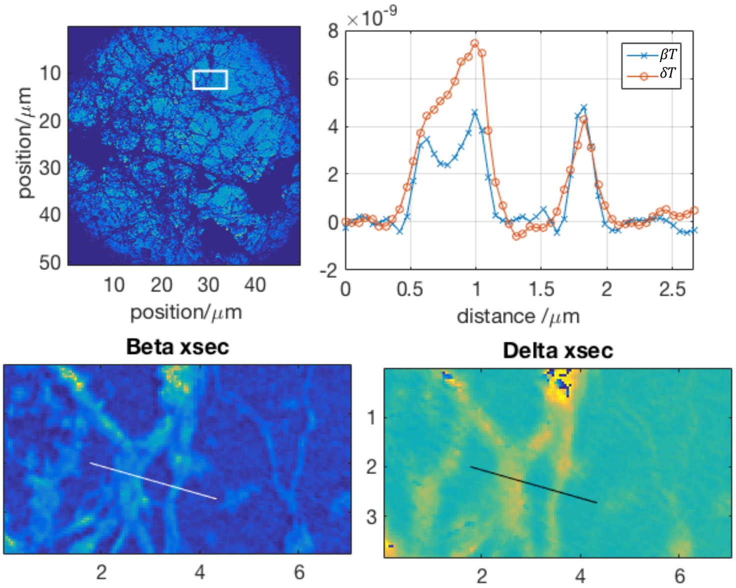

FIGURE 41: Sectional analysis of 14DIV neuron Southampton reconstruction, showing δ/β variation within a single feature that is yet different from δ/β of another feature. Top (left to right): Full image of the reconstruction in intensity, showing selected region for analysis boxed in white; plot of δT and βT along selected line segment. Bottom (left to right): Beta xsec graph shows selected region in amplitude with selected line segment; Delta xsec graph shows selected region in phase with selected line segment. All axes represent position, given in μm. The graph of δT and βT shows one feature that exhibits the pattern of similar δ/β on either side but different in the middle, and this feature is the wider of the two strands. $\delta/\beta \sim 1$ for the other strand, which is thin.

5.3 Discussion

As the two new reconstructions are of 7DIV neuron samples, though many fine, undifferentiated neurites can be seen, they are generally not yet fully-formed and differentiated neuron structural features as the cells are as not very far into development. The reliance on reconstruction to produce an image also means it is difficult to adjust the field of view of the scan, so it is difficult to return to image the same area once realignment has taken place. However, these reconstructed images provide a good opportunity to investigate whether δ and β information can be extracted from the data. In particular, the reconstruction of 7DIV neurons imaged at Southampton, shown in Figure 27, contains many thin, separated features with suitably high transmission that is suited for such analysis.

For features that appear relatively well-defined, δT and βT typically track similarly, and instances where there is significant difference between these two is sufficient to alert to a difference in appearance of a structure in the amplitude and phase data. This can be useful identifying tubular structures, be it hollow or filled with a different material.

δ/β is likely a key piece of information to be considered in this analysis, as the ratio δ/β is constant and unique for each element, and correspondingly, each material. Theoretically, this could be used to identify exact compounds in the sample if there is an extensive reference database of δ/β values for all possible materials in the sample. In practice, considering the range of δ/β values for different types of macromolecules has been more informative in indicating spatial distribution of content such as lipid and protein, which in turn may shed light on structural features.

In these neuron reconstructions, δ/β values from the initial analysis process (Figures 28 – 33) have been observed to be within the range of 1.7–3. Lipids often have δ/β values in this range, indicating that this may be the major content in the neuron samples. This would align with what happens during the fixing process, where multiple ethanol washes may have removed majority of the protein content, leaving behind lipids. However, there are certain regions where δ/β values fall within the range of proteins – proteins and amino acids usually have δ/β values in the vicinity of 1.5–2.0 suggesting that some protein content may remain intact despite the fixing process. This may also be a possible result the fixing process, particularly since the ethanol dehydration process was done slowly in order to keep as much structure intact as possible. There is also the possibility that the ethanol washes have left much of the protein content denatured, but still present in the sample.

While the initial analysis process is quick and can be used to generate δ/β data, care must be taken when considering δ/β values obtained from the data. Dr Brocklesby's analysis routine considers the data more carefully when fitting Gaussian distributions to the data in order to differentiate the background distribution from the signal. δT and βT values reported may sometimes be negative or 0, which can lead to low signal-to-noise ratio in the δ/β values calculated. Instead, to avoid these pitfalls it is better to consider δT and βT values and deduce the behaviour of δ/β where necessary.

From looking at sets of analysis using this method (Figures 35 – 41), there are several main observations. On the whole, δT and βT typically track similarly. This is particularly obvious when looking at a cross section that spans several strand-like features. However, there are certain strands for which $\beta T > \delta T$, which would give $\delta/\beta < 1$. This does not correspond to any straightforward values of δ/β for compounds such as protein or lipid. The origin for this observation is yet unclear, and may be worth looking into as part of further work.

An interesting observation from the results of applying Dr Brocklesby's analysis routine to the two sets of data (Figures 27 and 33) is that there are examples of δT and βT tracking differently along the cross-section of a feature such that the δ/β values are similar on either side of a feature and different in the middle. This is can be seen in Figures 37, 38, and 41. This behaviour often occurs across features that look like a thicker 'strand', which may correspond to the δ/β variation for a tubular structure – the material of the wall is different from the material in the center of the tubule.

The main observations from both analysis methods are very similar, though Dr Brocklesby's analysis routine is likely the more robust and sensitive of the two in handling the data from the reconstruction. Additionally, δT and βT analysis of structure and content proves to be significantly weaker in regions that appear web-like using both methods. This is likely due to of a combination of what appears to be poorer reconstruction in such regions, as well as the possibility that these web-like regions are in fact bundles of thinner neurites – often called neuronal processes – that are not resolved fully at this EUV wavelength.

Calculation of sample thickness is possible from equations 5.8 and 5.11. However, from observations of δ/β values and their changes, it can prove difficult to identify the correct material with appropriate δ and β values that give matching values of sample thickness, T. Instead, it may be more effective to observe differences in δT and βT and patterning of δ/β values to glean information about fine structures such as filopodia or neuronal processes as well as composition of structures.

Chapter 6

Conclusions and future work

6.1 Conclusions

Ptychography of 7DIV mouse neurons has been successfully performed on the EUV beamline at the University of Southampton and the beamline at the Artemis laser facility, and the reconstructions have been presented. For the ptychography experiments on the Artemis beamline, one experiment made used of a projection pinhole created by using an iris just upstream of the Al filters. While this method was demonstrated successfully, the reconstruction was poorer. The projection pinhole creates an illuminating probe that is much more smooth compared to the hard edge of the tophat function illumination probe that a physical pinhole would provide.

Work was concentrated on resolving multiple equipment issues and analysis of the reconstructed data to investigate the possibility of compositional analysis. Though the young neurons in the 7DIV stage have fewer fully formed characteristic neuron structural features, many thin neurites that have yet to differentiate can be seen, demonstrating that ptychography is able to provide new insight on structure and detailed features. These samples also offered an opportunity to explore analysis of the reconstruction data.

From analysis of the reconstructed data is clear that δ/β, the ratio between the coefficients of the complex refractive index, values would be ideal for identification against known compounds. Analysis results show that δ/β ratios correspond to that of proteins and lipids, and these can sometimes be observed in the pattern of a tubular structure. However, the extraction of δT and βT values where T is the sample thickness is a more robust way to observe δ/β behaviour, and several recurring patterns regarding δ/β behaviour have been observed.

This is a new method to image neurons with, and there is much unexplored potential in further discovering imaging capabilities and relating the phase information that ptychography recovers with biological structure and function.

6.2 Future work

Over the duration of this project, consecutive equipment issues significantly hindered progress and so exploration in further areas were limited by time constraints. There is room for improvement of the beamline with regard to modifications or addition of elements that would create a more robust experimental setup and allow for greater flexibility in variables, such as more comprehensive monitoring of pressure, pickoff mirrors for diagnostics, greater distance of travel in the motorised stages, and ease of mounting multiple samples. There are also several possible areas that could add substantially to the work of the research group, and some of these are described below.

6.2.1 Cooling coil

In addition to the measures described in section 4.5 that were taken to combat oil condensation on the cooled CCD surface, as part of exploring other methods to tackle this problem a cooling coil was designed and constructed. The cooling coil consists of a copper tube coiled multiple times, fitted with a stainless steel flange suitable for use with cryogenic liquids that allows the coil to be installed on the vacuum chamber, as well as a small metal funnel to allow for ease of pouring in liquids. It is planned for this copper coil to be filled with liquid nitrogen, such that it acts as a cold finger that will out-compete the cooled CCD surface as the coldest surface within the vacuum environment so that any oil vapour will condense on the coil instead of the CCD detector surface. Testing out the cooling coil has been delayed due to lack of auxiliary equipment for handling liquid nitrogen, but is a relatively straightforward modification to the vacuum chamber to trial. If suitable, this may significantly help with oil contamination risks.

6.2.2 Motorised beam stop

A modification planned for the current imaging beamline setup is the installation of a beam stop that can be moved into and out of the center beam, in front of the CCD, a common feature in synchrotron, FEL, or crystallography experiments. This will provide a physical method to increase the dynamic range of the CCD detector in addition to the HDR exposure routine for taking multiple images to acquire a diffraction pattern with high dynamic range. It is planned for this beam stop to be mounted via or near the CCD casing, and to be switched into position via a high-precision piezoelectric rotating stage. A physical beam stop rather than code that simulates the effect of a beam stop allows for different versions to be installed depending on suitability or availability. For example, the beam stop may be opaque or partially transmitting. With a rotating piezoelectric stage it may also be possible to mount several beam stops of varying sizes and switch in specific ones accordingly while remaining at vacuum, which would allow further flexibility in experimental conditions.

6.2.3 Projection pinhole with mask

As demonstrated in this thesis, an iris-created projection pinhole may not have a sufficiently sharp edge in the illuminating function in defines. This may result in poorer reconstruction. A projection pinhole of a different, perhaps irregular shape may help combat this. Alternatively, a mask can be placed close in front of the sample may help to give the required hard edge if the mask has a polygon shape.

6.2.4 Neurons in other developmental stages

There is still much to be explored with the imaging of developing mouse neurons, including imaging neurons samples at different developmental stages. The neurons imaged thus far have also been wild-type cells with no staining or fluorescent tagging. It would be interesting to perform EUV ptychography on samples that have been stained or transfected to see the effect after reconstruction.

6.2.5 Dosage and irradiation damage

An observation that has been made since successful imaging has been performed using this system at Southampton is that there is considerably less radiation damage in the samples imaged on the EUV beamline than those imaged on a synchrotron beamline, though the radiation dosage in the former is higher. This has yet to be studied in detail and the reason unknown, but could be a particularly interesting finding if true.

6.2.6 Compositional analysis

Further work in developing more robust and effective techniques for compositional analysis would add much value to ptychography as an imaging technique. A starting point could devising a reliable way to obtain δ/β values for any desired compound, including biological macromolecules. It may also be useful to consider the classes of proteins or lipids that may be present in developing cells. For example, cytoskeletal proteins such as actin and tubulin that form filamentous structures are proteins that are likely to be present in young neuron cells, as the cytoskeleton is important in cell growth and development. If these macromolecules can be identified, either by δ/β values, or by prior recombinant tagging, this would be a novel observation by x-ray ptychography.

Similar compositional analysis for ptychography carried out using other wavelengths such as 13 nm or wavelengths within the water window may also be highly informative.

Bibliography

[1] Ozcan, A., & McLeod, E. (2016). Lensless Imaging and Sensing. *Annual Review of Biomedical Engineering*, *18*(1), 77–102. https://doi.org/10.1146/annurevbioeng-092515-010849

[2] Abbey, B., Whitehead, L. W., Quiney, H. M., Vine, D. J., Cadenazzi, G. A., Henderson, C. A., … McNultyI. (2011). Lensless imaging using broadband X-ray sources. Nat Photon, 5(7), 420–424. http://dx.doi.org/10.1038/nphoton.2011.125

[3] Baksh, P. Ptychographic Imaging of Real Biological Samples using a High Harmonic and Synchrotron Source, PhD Thesis, University of Southampton, 2016

[4] Odstrcil, M. Coherent Diffractive Imaging Using Table-top Source, PhD Thesis, University of Southampton, 2016

[5] Weisenburger, S., & Sandoghdar, V. (2014). Light Microscopy: An ongoing contemporary revolution, 1–37. https://doi.org/10.1080/00107514.2015.1026557

[6] Urban, K. W. (2008) Studying atomic structures by aberration-corrected transmission electron microscopy. *Science*, 321(5888), 506-510. https://doi.org/10.1146/annurev-bioeng-061008-124811

[7] Thompson, R. F., Walker, M., Siebert, C. A., Muench, S. P., & Ranson, N. A. (2016). An introduction to sample preparation and imaging by cryo-electron microscopy for structural biology. *Methods*, *100*, 3–15. https://doi.org/10.1016/j.ymeth.2016.02.017

[8] Boustany, N. N., Boppart, S. A., & Backman, V. (2010). Microscopic Imaging and Spectroscopy with Scattered Light. *Annual Review of Biomedical Engineering*, *12*, 285–314.

[9] Attwood, D. Soft x-rays and extreme ultraviolet radiation: principles and applications. Cambridge University Press, 1999.

[10] E.M. Gullikson B.L. Henke and J.C. Davis. THE CENTRE FOR X-RAY OPTICS, 1995-2014. http://henke.lbl.gov/optical_constants/.

[11] Seaberg, M. D., Adams, D. E., Townsend, E. L., Raymondson, D. A., Schlotter, W. F., Liu, Y., … Murnane, M. M. (2011). Ultrahigh 22 nm resolution coherent diffractive imaging using a desktop 13 nm high harmonic source. *Optics Express*, *19*(23), 22470–22479. https://doi.org/10.1364/OE.19.022470

[12] Ersoy, O. K. Diffraction, Fourier optics and Imaging, Wiley Interscience, 2007

[13] Miao, J., Ishikawa, T., Robinson, I. K., & Murnane, M. M. (2015). Beyond crystallography: Diffractive imaging using coherent x-ray light sources. *Science*, *348*(6234), 530 LP-535. http://science.sciencemag.org/content/348/6234/530.abstract

[14] Bunk, O., Dierolf, M., Kynde, S., Johnson, I., Marti, O., & Pfeiffer, F. (2008). Influence of the overlap parameter on the convergence of the ptychographical iterative engine. *Ultramicroscopy*, *108*(5), 481–487.

[15] Guizar-Sicairos, M., & Fienup, J. R. (2008). Phase retrieval with transverse translation diversity: a nonlinear optimization approach. *Optics Express*, *16*(10), 7264–7278. https://doi.org/10.1364/OE.16.007264

[16] Maiden, A. M., Humphry, M. J., Sarahan, M. C., Kraus, B., & Rodenburg, J. M. (2012). An annealing algorithm to correct positioning errors in ptychography. *Ultramicroscopy*, *120*, 64–72. https://doi.org/http://dx.doi.org/10.1016/j.ultramic.2012.06.001

[17] Zhang, F., Peterson, I., Vila-Comamala, J., Diaz, A., Berenguer, F., Bean, R., … Rodenburg, J. M. (2013). Translation position determination in ptychographic coherent diffraction imaging. *Optics Express*, *21*(11), 13592–13606. https://doi.org/10.1364/OE.21.013592

[18] Maiden, A.M., Humphry, M. J., & Rodenburg, J. M. (2012).Ptychographic transmission microscopy in three dimensions using a multi-slice approach. *J. Opt. Soc. Am.* A 29, 1606-1614.

[19] Sayre, D. (1952) Some Implications of a theorem due to shannon. *Acta Crystallogr.* 5(6), 843–843

[20] Nyquist, H., "Certain topics in telegraph transmission theory," *Transactions of the American Institute of Electrical Engineers*. 47, 617–644 (1928).

[21] Shannon, C. E., "Communication in the presence of noise," *Proceedings Institute of Radio Engineers*. 37(1), 10–21 (1949).

[22] Bates, R.H.T. & Fright, W.R. (1983). Composite two-dimensional phase-restoration procedure. *JOSA*, 73(3), 358-365,.

[23] Miao, J., & Sayre, D. (2000). On possible extensions of X-ray crystallography through diffraction-pattern oversampling. *Acta Crystallographica Section A: Foundations of Crystallography*, 56(6), 596-605.

[24] Gerchberg, R. W. (1972). A practical algorithm for the determination of phase from image and diffraction plane pictures. *Optik*, 35-237.

[25] Fienup, J. R. (1982). Phase retrieval algorithms: A comparison, *Appl. Opt.*, 21, 2758–2769.

[26] Marchesini, S., He, H., Chapman, H. N., Hau-Riege, S. P., Noy, A., Howells, M. R., ... Spence, J. C. H. (2003). X-ray image reconstruction from a diffraction pattern alone. *Physical Review B - Condensed Matter and Materials Physics*, 68(14), 1401011-1401014.

[27] Rodenburg, J. M., & Faulkner, H. M. L. (2004). A phase retrieval algorithm for shifting illumination. *Applied Physics Letters*, *85*(20), 4795–4797. https://doi.org/10.1063/1.1823034

[28] Maiden, A. M., & Rodenburg, J. M. (2009). An improved ptychographical phase retrieval algorithm for diffractive imaging. *Ultramicroscopy*, *109*(10), 1256–1262. http://dx.doi.org/10.1016/j.ultramic.2009.05.012

[29] Howells, M. R., Beetz, T., Chapman, H. N., Cui, C., Holton, J. M., Jacobsen, C. J., … Starodub, D. (2009). An assessment of the resolution limitation due to radiation-damage in x-ray diffraction microscopy. *Journal of Electron Spectroscopy and Related Phenomena*, *170*(1–3), 4–12.

[30] Elser, V., Rankenburg, I., & Thibault, P. (2007). Searching with iterated maps. *Proceedings of the National Academy of Sciences*, 104(2), 418–423. https://doi.org/10.1073/pnas.0606359104

[31] Corkum, P. B. (1993). Plasma perspective on strong field multiphoton ionization. Physical Review Letters, 71(13), 1994–1997. Retrieved from https://link.aps.org/doi/10.1103/PhysRevLett.71.1994

[32] Miller, Benjamin K., "Classical Analysis of High Harmonic Generation" (2015). *Undergraduate Honors Theses*, University of Colorado, Boulder. Paper 983.

[33] Butcher, T. J. Methods for Increased Energy and Flux in High Harmonic Generation. PhD thesis, University of Southampton, 2012. http://www.orc.soton.ac.uk/viewpublication.html?pid=5383.

[34] Lindner, F., Stremme, W., G. Schätzel, M., Grasbon, F., Paulus, G., Walther, H., … Strüder, L. (2003). High-order harmonic generation at a repetition rate of 100 kHz. *Physical Review A, v.68, 013814-013814* (Vol. 68). https://doi.org/10.1103/PhysRevA.68013814

[35] Lindner, F., Paulus, G. G., Walther, H., Baltuška, A., Goulielmakis, E., Lezius, M., & Krausz, F. (2004). Gouy Phase Shift for Few-Cycle Laser Pulses. *Physical Review Letters*, *92*(11), 113001. Retrieved from https://link.aps.org/doi/10.1103/PhysRevLett.92.113001

[36] Heyl, C., Arnold, C., Couairon, A., & L'Huillier, A. (2017). Introduction to macroscopic power scaling principles for high-order harmonic generation. Journal of Physics B: Atomic, Molecular and Optical Physics (Vol. 50). https://doi.org/10.1088/1361-6455/50/1/013001

[37] Falcão-Filho, E. L., Gkortsas, V. M., Gordon, A., & Kärtner, F. X. (2009). Analytic scaling analysis of high harmonic generation conversion efficiency. *Optics Express*, 17(13), 11217–11229. https://doi.org/10.1364/OE.17.011217

[38] Kazamias, S., Douillet, D., Valentin, C., Lefrou, T., Grillon, G., Mullot, G., … Balcou, P. (2003). Optimization of the focused flux of high harmonics. Eur. Phys. J. D, 26(1), 47–50. Retrieved from https://doi.org/10.1140/epjd/e2003-00083-y

[39] [Biological_neuron.gif]. (2017). By Geetika saini [CC BY-SA 4.0 (https://creativecommons.org/licenses/by-sa/4.0)], from Wikimedia Commons.

https://upload.wikimedia.org/wikipedia/commons/4/4a/Biological_neuron.gif

[40] Alberts, B., Johnson, A., Lewis, J., Raff, M., Roberts, K., & Walter, P. (2002) Molecular Biology of the Cell, 4th Edition. New York: Garland Science. Available from: https://www.ncbi.nlm.nih.gov.books/NBK21054